The Astrophysical Journal, 943:124 (21pp), 2023 February 1 https://doi.org/10.3847/1538-4357/ac9799

COCONUT, a Novel Fast-converging MHD Model for Solar Corona Simulations. II. Assessing the Impact of the Input Magnetic Map on Space-weather Forecasting at Minimum of Activity

Barbara Perri[1], Błażej Kuźma[1], Michaela Brchnelova[1], Tinatin Baratashvili[1], Fan Zhang[1], Peter Leitner[2], Andrea Lani[1], and Stefaan Poedts[1,3]
[1] Centre for Mathematical Plasma Astrophysics/Department of Mathematics, KU Leuven, 3001 Leuven, Belgium; barbara.perri@kuleuven.be
[2] Institute of Physics, University of Graz Universitätsplatz 5, 8010 Graz, Austria
[3] Institute of Physics, University of Maria Curie-Skłodowska, Pl.M. Curie-Skłodowskiej 5, 20-031 Lublin, Poland
Received 2022 May 9; revised 2022 September 26; accepted 2022 October 2; published 2023 February 1

Abstract

This paper is dedicated to the new implicit unstructured coronal code COCONUT, which aims at providing fast and accurate inputs for space-weather forecasting as an alternative to empirical models. We use all 20 available magnetic maps of the solar photosphere covering the date of 2019 July 2, which corresponds to a solar eclipse on Earth. We use the same standard preprocessing on all maps, then perform coronal MHD simulations with the same numerical and physical parameters. We conclude by quantifying the performance of each map using three indicators from remote-sensing observations: white-light total solar eclipse images for the streamers' edges, EUV synoptic maps for coronal holes, and white-light coronagraph images for the heliospheric current sheet. We discuss the performance of space-weather forecasting and show that the choice of the input magnetic map has a strong impact. We find performances between 24% and 85% for the streamers' edges, 24%–88% for the coronal hole boundaries, and a mean deviation between 4° and 12° for the heliospheric current sheet position. We find that the HMI runs perform better on all indicators, with GONG-ADAPT being the second-best choice. HMI runs perform better for the streamers' edges, and GONG-ADAPT for polar coronal holes, HMI synchronic for equatorial coronal holes, and the streamer belt. We especially illustrate the importance of the filling of the poles. This demonstrates that the solar poles have to be taken into account even for ecliptic plane previsions.

Unified Astronomy Thesaurus concepts: Solar corona (1483); Solar wind (1534); Magnetohydrodynamics (1964); Solar magnetic fields (1503); Space weather (2037)

1. Introduction

With societies increasingly relying on technology, we now have the critical need to anticipate major malfunctioning or even catastrophic events in order to protect civilians. Some of the most significant risks have been events coming from space (Schrijver et al. 2015). Highly energetic particles can be accelerated at the Sun or by magnetic structures in the interplanetary medium (Reames 2013), reaching energies that allow them to disrupt satellites, jeopardize astronauts' lives, and interact with the Earth's atmosphere, leading to communication blackouts (Bothmer & Daglis 2007). These events are called solar energetic particle (SEP) events; for more details, see the review by Reames (2021). Magnetic storms are another type of event caused by coronal mass ejections (CMEs) interacting with Earth's magnetosphere (Pulkkinen 2007), resulting in currents in the Earth's crust that cause severe electrical damage to installations (Pirjola 2005). Space-weather forecasting's mission is to anticipate these disruptive events by simulating the chain of causality from the Sun to Earth and issue forecasts (Temmer 2021). The key to reliable previsions is not only to be able to accurately model the transient phenomena, but to also describe precisely the interplanetary medium in which they propagate and with which they interact before reaching Earth (Shen et al. 2022). Although many effects influence the transients' propagation (Lavraud & Rouillard 2014), they can be linked back to two main physical ingredients. On the one hand, the magnetic field bathes the interplanetary medium, following a complex pattern influenced by the Parker spiral at large scales and fluctuations at small scales (Owens & Forsyth 2013). Its long-term variations are linked to the 11 yr cycle of solar activity generated inside the star by the dynamo effect (Brun & Browning 2017), while its short-term variations may be linked to the convection at the surface of the star (Fargette et al. 2021). On the other hand, the solar wind flows the interplanetary medium with continuous ejected plasma, and shapes large-scale structures with shock regions caused by the interaction between slow and fast wind (stream interacting regions (SIRs; McComas et al. 2003, 2008).

It is only natural that an increasing number of countries are then developing frameworks for space-weather forecasting: ENLIL and SWMF for the United States (Odstrcil 2003; Tóth et al. 2012), SUSANOO for Japan (Shiota et al. 2014), and VSWMC for Europe (Poedts et al. 2020a). All these frameworks are based on the same principle: since it is impossible to use one model to cover the diversity of scales between the Sun and Earth, the best approach is to couple models dedicated to a specific region and physics. For instance, the VSWMC framework uses photospheric measurements of the solar magnetic field as input, then semiempirical (WSA) and magnetic (PFSS + SCS) extrapolations from 1–21.5 $R_\odot$, and then the heliospheric propagator EUHFORIA to compute physical quantities from 0.1 au to Earth and beyond (the typical outer boundary condition is set at 2 au) (Pomoell & Poedts 2018). The first steps in this chain of the

model, namely, the magnetic map chosen as input and the coronal model used to compute the boundary conditions at 0.1 au, are thus crucial as they determine the initialization of the rest of the models. They are also at the core of the two main physical ingredients that will disturb the transients' propagation: the magnetic maps are a direct measurement of the solar activity, and the solar corona is the siege of the acceleration of the solar wind (Cranmer & Winebarger 2019). To better model these sensitive effects, we used alternative magneto-frictional and MHD coronal models with more physics incorporated within, in order to replace and improve the semiempirical and potential extrapolations up to 0.1 au (Poedts et al. 2020b). Within the MHD models, there are other levels of complexity, such as the number of dimensions that are considered (1D versus 3D) (Pinto & Rouillard 2017; Mikić et al. 2018), or the level of sophistication to describe the coronal heating (polytropic versus Alfvén waves) (Perri et al. 2018; Réville et al. 2020). There are even models that go beyond the fluid approximation by taking into account the multispecies nature of the solar wind (van der Holst et al. 2014; Chhiber et al. 2021). This approach has already proven successful for specific test cases (Samara et al. 2021). The dilemma is that as we apply more and more physics, what we gain in accuracy is lost in speed and robustness. As space-weather forecasting requires all three qualities, we have developed a new coronal model to satisfy all these constraints. The COCONUT (COolfluid COroNal UnsTructured) coronal model uses the time-implicit methods from the COOLFluiD framework, which allows it to be up to 35 faster than typical explicit codes while achieving the same level of accuracy (Perri et al. 2022). It also has the advantage of using unstructured meshes instead of regular grids, which allows it to avoid degeneracy at the poles and thus provide more accuracy in this region. As more and more coronal models begin to be suited for space-weather forecasting, another important goal of the community is to derive metrics to evaluate the quality of the models and thus retain the best parameters for previsions (Lionello et al. 2009; Badman et al. 2022; Samara et al. 2022; Wagner et al. 2022).

This paper focuses in particular on the choice of the input magnetic map, as it is the driver of the entire numerical simulation. Many studies have tried to bridge the gap between various magnetic maps from different observatories, but no consensus could be found behind these observations (Riley et al. 2014; Virtanen & Mursula 2017). This is essentially due to the lack of a multi-vantage point, for example, no 360° view of the Sun is available at all times since the breakdown of STEREO-B. New studies suggest that the choice of the input map and its preprocessing would significantly change the description of the coronal structure (Yeates et al. 2018), and thus of the SIRs and CME propagation (Riley & Ben-Nun 2021; Samara et al. 2021). For this reason, an increasing number of studies focus on trying to assess the impact of the choice of the input map on the resulting coronal structure (Petrie 2013; Wallace et al. 2019; Caplan et al. 2021; Li et al. 2021). However, most of these studies rely on PFSS extrapolations to describe the coronal magnetic field, while MHD would be more physical, especially further away from the star (Réville et al. 2015). MHD studies have begun to be conducted, but so far mostly for a few codes, which are the MAS and AWSoM codes (Linker et al. 2017; Jin et al. 2022). For all magnetic maps, the greatest uncertainty lies in the solar poles, as the viewpoint from Earth and satellites in the ecliptic plane does not allow for precise global measurement. Only local observations by Hinode or soon Solar Orbiter allow us to retrieve high-resolution information from the solar poles (Tsuneta et al. 2008). There are however indirect techniques that can be used such as microwave imaging observations (Gopalswamy et al. 2012) or the Zeeman effect (Ito et al. 2010). This is problematic for global coronal models, as it leads to huge uncertainties on the open solar flux (Riley et al. 2019) and therefore underestimation of the magnetic field at Earth (Owens et al. 2008; Jian et al. 2015). The solar poles have been known to greatly influence the dynamics of the corona by affecting the initial mass function (IMF) field strength, the HCS excursions, and the wind speed through the polar coronal holes (Petrie 2015). However, the impact of solar pole modeling in space-weather forecasting has not been properly quantified. This is made even more difficult by the fact that most models do not include the solar poles in the heliospheric part (Pomoell & Poedts 2018), and sometimes even in the coronal part (Pinto & Rouillard 2017), thus implicitly assuming that the influence of the poles can be neglected. Our goal is to test these assumptions, first for a well-documented case of the minimum of activity on 2019 July 2. The choice of the minimum of activity allows us to focus on the influence of the poles rather than the active regions, which is also made possible by our unstructured mesh approach, allowing for fully including the poles within the computational domain. The choice of the date allows us to have precise pictures of the solar corona thanks to a total solar eclipse as seen from Earth.

This paper is organized as follows. In Section 2, we provide an overview of the magnetic maps that are used as input for our simulations (all 20 maps are publicly available for the 2019 July 2 total solar eclipse), explaining, in particular, their differences in spectral line selection, resolution, and pole-filling techniques. In Section 3, we present our numerical model COCONUT, which uses these magnetic maps in order to simulate the solar wind in the corona up to 0.1 au. We describe the physical as well as the numerical parameters that are used to constrain the simulations. We also discuss the preprocessing of the maps for quantifying the difference in the initialization of the simulations. In Section 4, we analyze the results of the 20 corresponding simulations that have been performed. We use three different observational data available for this date to validate the results: we compare magnetic field lines to white-light images (Section 4.1), open and closed magnetic field line distribution to coronal hole detection in EUV (Section 4.2), and the position of the heliospheric current sheet (HCS) to the streamer belt (SB) white-light reconstruction (Section 4.3). In Section 5, we discuss the implications for space-weather forecasting. We begin by comparing the resulting magnetic field configuration at 0.1 au with the typical WSA + PFSS + SCS model currently used for coupling with EUHFORIA (Section 5.1). We then assemble all our results into a scoreboard for this event, determining which magnetic map allows our model to fit the observational data the best (Section 5.2). We especially focus on the pole-filling techniques and their implication for forecasting (Section 5.3). Finally, in Section 6 we present the conclusions of our study and present perspectives for future work.

2. Description of the Magnetic Maps

Our simulations are data driven in the sense that the inner boundary condition for the radial magnetic field B_r is imposed based on a synoptic map derived from solar observations of the

Table 1
Properties of the Synoptic Magnetic Maps Used in This Study

Source	Spectral Line (nm)	Type	Resolution	Units	*Y*-axis	Pole Filling	Time Span	CRs
WSO	Fe 525	LOS	73×30	μT	$\sin\theta$ or θ	None	1976.3 -	1642 -
GONG	Ni 676.8	Pseudo-radial	360×180	G	$\sin\theta$	Cubic-polynomial fit	2006.7 -	2047 -
HMI	Fe 617.3	Pseudo-radial	3600×1440	G	$\sin\theta$	None	2010.4 -	2096 -
GONG-ADAPT	Ni 676.8	Pseudo-radial	360×180	G	θ	Flux-transport models	2007.002 -	2052 -

Note. For each source, we specify the observed spectral line, type of magnetic field, resolution of the map, units of the magnetic field, type of *y*-axis that has been used, pole-filling technique, available time span, and the corresponding Carrington rotations (CRs). For the source of the magnetic maps, please check the Acknowledgments section.

photospheric magnetic field. There are also models that are fully data driven because they use the three components of vector magnetograms as an inner boundary condition, along with velocity components V_θ and V_φ. The number of Dirichlet conditions is then determined by the directions of the characteristic waves going in and out of the photosphere (Wu et al. 2006; Yalim et al. 2017; Singh et al. 2018). Such methods are more difficult to implement within our unstructured grid and implicit solver, so this remains beyond the scope of this study and will be considered for future extensions of the code. For the selected date (2019 July 2), we used all publicly available processed synoptic maps from four different sources: WSO (Wilcox Solar Observatory), GONG (Global Oscillation Network Group), HMI (Helioseismic and Magnetic Imager), and GONG-ADAPT (Air Force Data Assimilative Photospheric Flux transport). Links to their corresponding downloadable sources are shown in the Acknowledgments section. A summary of their main properties can be found in Table 1. In this section, we explain the differences between these different maps, focusing on the observation techniques, the assembly methods, and the pole-filling methods.

All the maps were obtained through magnetographs, although the latter use various techniques in different contexts. The first difference is the observed spectral line, as seen in Column 2 of Table 1. At WSO, a Babcock solar magnetograph records the Zeeman polarization in the wings of an absorption line of iron at 5250 Å (Ulrich 1992). It is the longest homogeneous series of observations with the same instrumentation, which has been used since 1976. GONG uses interferometric techniques in order to measure the opposite states of polarization of the Ni I 6768 Å line, which is based on six stations around the world since 2006. HMI is an instrument on board the Solar Dynamics Observatory (SDO) satellite launched in 2010, which observes the full solar disk in the Fe I absorption line at 6173 Å. It was calibrated using the Michelson Doppler Imager (MDI) on board the Solar and Heliospheric Observatory (SOHO). It can also record 3D vector magnetograms. Finally, the GONG-ADAPT maps are based on the GONG observations, so also rely on the Ni I 6768 Å line. These differences in spectral lines technically mean that the maps are not representing the magnetic field at the same height, which can result in slightly different structures. The third column refers to the fact that all observatories measure the line-of-sight (LOS) component of the magnetic field. However, some of them convert this value into a pseudo-radial field under the assumption that the total field is radial. Column 4 shows another important difference between the maps, which is their resolution. WSO is the lowest-resolution device with only a 3′ aperture size, which results in maps of 73 pixels in longitude and 30 pixels in latitude. GONG (and consequently GONG-ADAPT) provides map products with 360 pixels in longitude and 180 pixels in latitude. Finally, HMI has the best resolution thanks to the fact that it is in space, with a 1″ resolution, and provides high-resolution maps with 3600 pixels in longitude and 1440 pixels in latitude. We also note in Column 5 that the units are mostly in Gauss, except for the WSO maps, which are in microTeslas. Column 6 shows another important geometric parameter, which is the type of *y*-axis used. "θ" means that the pixels are in equal steps of latitude, which is the case for GONG-ADAPT between $-90°$ and $90°$, and a possible option for WSO between $-70°$ and $70°$. "$\sin\theta$" means that the pixels are in equal steps of sine latitude (to account for the fact that the poles are difficult to measure from the point of view of the ecliptic plane), which is the case for GONG and HMI between -1 and 1, and an option for WSO between $-14.5/15$ and $14.5/15$. We should also note that over the years, various processes have been applied to the data or have been highly recommended. In this study, we took the maps as they were, and chose to not apply any corrections. WSO for example had several periods with sensitivity issues, some of them having been recalibrated (between 2000 November and 2002 July, and between 2016 December 16 and 2017 May 18). There is also the general problem of saturation described in Svalgaard et al. (1978) and updated in Svalgaard (2006). Please note that the difference between GONG and GONG-ADAPT is also mostly some post-processing, as we will explain in the next paragraph. This modification history is not always made public, and thus can produce differences based on the date on which the data were downloaded and processed. For more details about the instruments, the reader can also refer to the reviews of Riley et al. (2014) and Virtanen & Mursula (2017).

Another important difference to discuss is the way the synoptic maps are assembled, and the very definition of a synoptic map in the first place. A synoptic map means that the full surface of the Sun is covered in 360°. However, it does not guarantee that all data used to create this full view were taken at the same time (this would be called a synchronic map). In reality, most of the maps are assembled using data at different dates, thus producing diachronic maps. For the WSO map, the full-disk images of the Sun are remapped over a month into Carrington longitudes, which means that there is a 27 day difference on average between data at 0° and 360° on the map. The HMI map follows the same idea, except that the better resolution allows averaging 20 magnetograms for each Carrington longitude. More precisely, individual pseudo-radial magnetograms are remapped on a very high-resolution Carrington coordinate grid. For each Carrington longitude, the 20 magnetograms closest in time to the central meridian passage (within 2°) for that longitude are selected and averaged. The result is that the effective temporal width of

the HMI synoptic map is about 3 hr. The choice of a constant number of contributing magnetograms allows for minimizing the variation in the noise over the entire map. A two-dimensional Gaussian function (whose width is 3 pixels) is then applied to high-resolution remapped data to reduce the spatial resolution before generating the high-resolution synoptic maps.[4] The HMI daily update synchronic frames provide a more up-to-date version of the synoptic map with the first 120° being replaced by the daily full-disk observation at the corresponding date from the twenty 720s magnetograms obtained between 10:00 and 14:00 UT, which helps reduce the time gap between data and allows taking into account fast-evolving structures. The origin of the frame is adjusted so that the newest data will appear on the left of the 360° map. We refer to this frame as the synchronic frame throughout the rest of this article. This does not mean that the full map is synchronic, but it is chosen so that the central meridian of the given date is always at 60° in longitude from the left-leading edge. Within this set of maps, we would like to take some time to describe more precisely some subsets of the maps. Within the GONG products, there are five different synoptic maps available. Two of them are integral magnetogram synoptic maps, and follow the same idea as described before: the mrmqs and mrnqs maps are built using data from the full Carrington rotation. To derive a map of the full-Sun magnetic field, fully calibrated 1 minute full-disk photospheric magnetograms from GONG's six sites are used. The first step is that the 1 minute images from the GONG network are merged to give continuous minute-by-minute coverage of the field. Then the merged images are remapped into longitude (measured from the central meridian) and sine latitude. Next, these remapped images are shifted to the Carrington frame and merged with a weighted sum to form a full surface picture of the solar magnetic field. Weighting factors take the form of a cosine to the power 4 of the longitude to ensure that measurements taken at a particular Carrington time contribute the most to that Carrington longitude in the final synoptic map.[5] The three others are synchronic frames magnetogram synoptic maps. This is especially visible when we plot all the maps in Figure 1. The mrbqj product called the Janus maps are similar to the HMI synchronic frame maps: the left 60° in longitude between −60° and 60° in latitude are updated using classic synoptic information, thus resulting in a composite magnetogram. However, in the case of the mrbqs and mrzqs products, this means that the 60° to the left of the map have not crossed the central meridian, and are thus not updated for the current Carrington rotation. Then, there is another distinction made between the zero-point corrected products (mrzqs, mrnqs) and the standard products (mrbqs, mrbqj, mrmqs): these maps have corrections at the poles to obtain a better estimate of the global magnetic flux. This can be seen in Figure 1 where the southern pole negative polarity is enhanced for GONG mrzqs and GONG mrnqs. Within the GONG-ADAPT map, there are actually 12 realizations produced. The differences rely on the various models used to try to approximate a synchronic map (Hickmann et al. 2015): here, GONG full-disk magnetograms are processed using forward modeling to account for differential rotation, meridional circulation, and supergranulation. Combined with data assimilation, this leads to a model ensemble of 12 realizations at the time of observation. All these different realizations are plotted in Figure 2 for 2019 July 2 in order to show the differences for a minimum of activity.

For the ease of the reader, we have summarized the main properties of the various GONG products in Table 2. Not all of these products were necessarily designed to be used as inputs for coronal modeling and space-weather previsions. The recommended products are the zero-point corrected ones (mrzqs and mrnqs), but for practical reasons, it turns out that some facilities still use the non-corrected synchronic products (mrbqs) (Poedts et al. 2020a), which makes them still relevant to study. The Janus maps were designed to more closely reproduce sudden changes in magnetic flux in the solar disk facing Earth. This makes them more precise but also possibly more unstable because they are noisier. Finally, the integral maps in the Carrington frame were not necessarily designed as an operational product, but they are closer to the HMI map, and we found it interesting to adopt an unbiased approach and test all of these maps for our model.

Finally, the maps may have been created using different techniques to fill the solar poles. The solar poles are currently not clearly visible with an extended range of latitudes by any magnetograph because all of them are located in the ecliptic plane, perpendicular to the poles. This will change with Solar Orbiter, which is scheduled to go 30° out of the ecliptic plane around 2025, in order to provide more detailed global pictures of the solar poles with an extended range of accessible latitudes. In the meantime, magnetic maps need to use extrapolation techniques if they want to improve the description of the poles. In the set that we are studying, we can see in Table 1 that the HMI map has not been corrected for the poles. Neither has the WSO map, but since it does not provide data between −70° and −90°, and 70° and 90°, we perform a linear extrapolation to fill these gaps. This means that the WSO map is going to have the least accurate information about the solar poles due to instrument limitations, since all data above 55° of latitude come from only one 3′ pixel. The GONG map performs a cubic-polynomial fit. Finally, GONG-ADAPT has the most sophisticated model, which takes into account flux transport to increase the concentration of the magnetic field at the poles because of the modeled meridional circulation.

3. Description of the COCONUT Code

COCONUT is a 3D MHD coronal model based on a fully implicit solver for finite volume methods on unstructured grids. The solver is part of the COOLFluiD framework (Kimpe et al. 2005; Lani et al. 2005, 2006, 2013), designed for scientific heterogeneous high-performance computing of multi-physics applications, including astrophysical plasmas (Lani et al. 2014; Alvarez Laguna et al. 2016; Maneva et al. 2017; Alonso Asensio et al. 2019; Alvarez Laguna et al. 2019). We refer the reader to Perri et al. (2022) for a complete description of the COCONUT code. We focus here on its main physical and numerical features.

3.1. Equations and Physical Parameters

We solve the ideal MHD equations in conservation form in Cartesian coordinates (more details are given in

[4] http://jsoc.stanford.edu/HMI/LOS_Synoptic_charts.html
[5] https://gong.nso.edu/data/dmac_magmap/

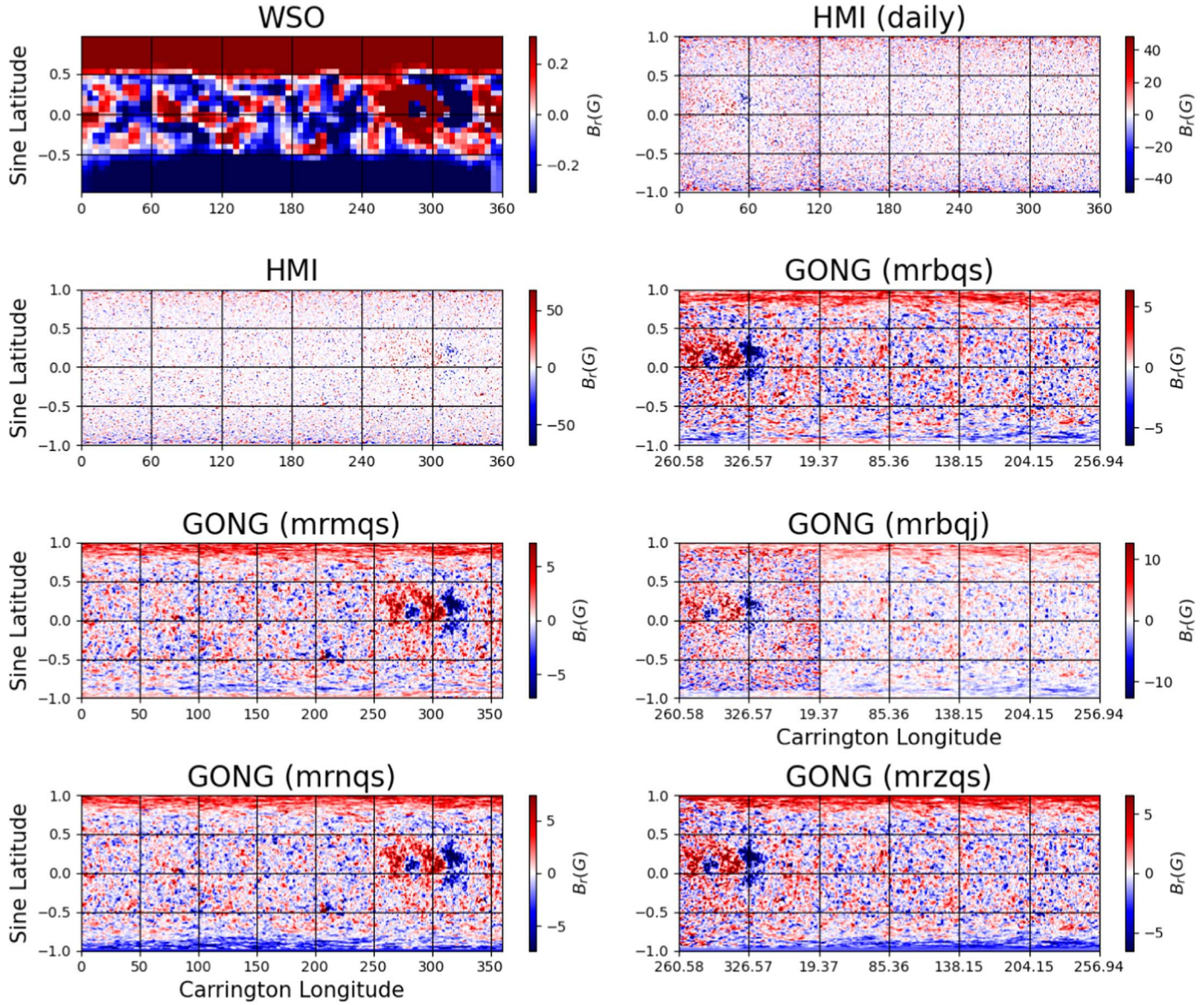

Figure 1. Comparison of synoptic maps for 2019 July 2 (CR 2219). From top to bottom, and then left to right: WSO, HMI, GONG (mrmqs), GONG (mrnqs), HMI (synchronic), GONG (mrbqs), GONG (mrbqj), and GONG (mrzqs). The first column shows Carrington frame synoptic maps, while the second column shows maps with longitude converted to the Carrington longitude for CR 2219. All data are in their original resolution and axis (longitude–sine-latitude). The ranges of the color bars have been set to plus and minus of the maximum of the field divided by 10, in order to have positive polarities in red and negative polarities in blue, as well as a good balance between small- and large-scale structures.

Yalim et al. (2011); Lani et al. (2014)):

$$\frac{\partial}{\partial t}\begin{pmatrix}\rho\\ \rho\boldsymbol{v}\\ \boldsymbol{B}\\ E\\ \rho\\ \phi\end{pmatrix}+\boldsymbol{\nabla}\cdot\begin{pmatrix}\rho\boldsymbol{v}\\ \rho\boldsymbol{v}\boldsymbol{v}+\mathbf{I}\left(p+\frac{1}{2}|\boldsymbol{B}|^2\right)-\boldsymbol{B}\boldsymbol{B}\\ \boldsymbol{v}\boldsymbol{B}-\boldsymbol{B}\boldsymbol{v}+\mathbf{I}\underline{\phi}\\ \left(E+p+\frac{1}{2}|\boldsymbol{B}|^2\right)\boldsymbol{v}-\boldsymbol{B}(\boldsymbol{v}\cdot\boldsymbol{B})\\ V_{ref}^2\boldsymbol{B}\end{pmatrix}=\begin{pmatrix}0\\ \rho\boldsymbol{g}\\ 0\\ 0\\ \rho\boldsymbol{g}\cdot\boldsymbol{v}\\ 0\end{pmatrix}, \quad (1)$$

in which E is the total energy, $\boldsymbol{B}$ is the magnetic field, $\boldsymbol{v}$ the velocity, $\boldsymbol{g}$ the gravitational acceleration, ρ the density, and p is the thermal gas pressure. The gravitational accelerati on is given by $\boldsymbol{g}(r) = -(GM_\odot/r^2)\hat{\boldsymbol{e}}_r$ and the identity dyadic $\mathbf{I} = \hat{\boldsymbol{e}}_x \otimes \hat{\boldsymbol{e}}_x + \hat{\boldsymbol{e}}_y \otimes \hat{\boldsymbol{e}}_y + \hat{\boldsymbol{e}}_z \otimes \hat{\boldsymbol{e}}_z$.

Since the ideal MHD equations are scale independent, they are implemented in COOLFluiD in dimensionless form. The following basis set $\{\ell_0, \rho_0, B_0\}$ of code units Q_0 is used to adimensionalize any physical quantity Q as $\tilde{Q} = Q/Q_0$: the unit length $\ell_0 = R_\odot = 6.95 \times 10^{10}$ cm, unit mass density $\rho_0 = \rho_\odot = 1.67 \times 10^{-16}$ g cm^{-3}, and $B_0 = 2.2$ G, a typical value for the background solar dipole field all represent solar surface values. All other code units are composed of combinations of the three base units, such as unit pressure $P_0 = \rho_0 V_0^2$ and gravitational acceleration $g_0 = V_0^2/\ell_0$ with $V_0 = B_0/\sqrt{\mu_0\rho_0}$.

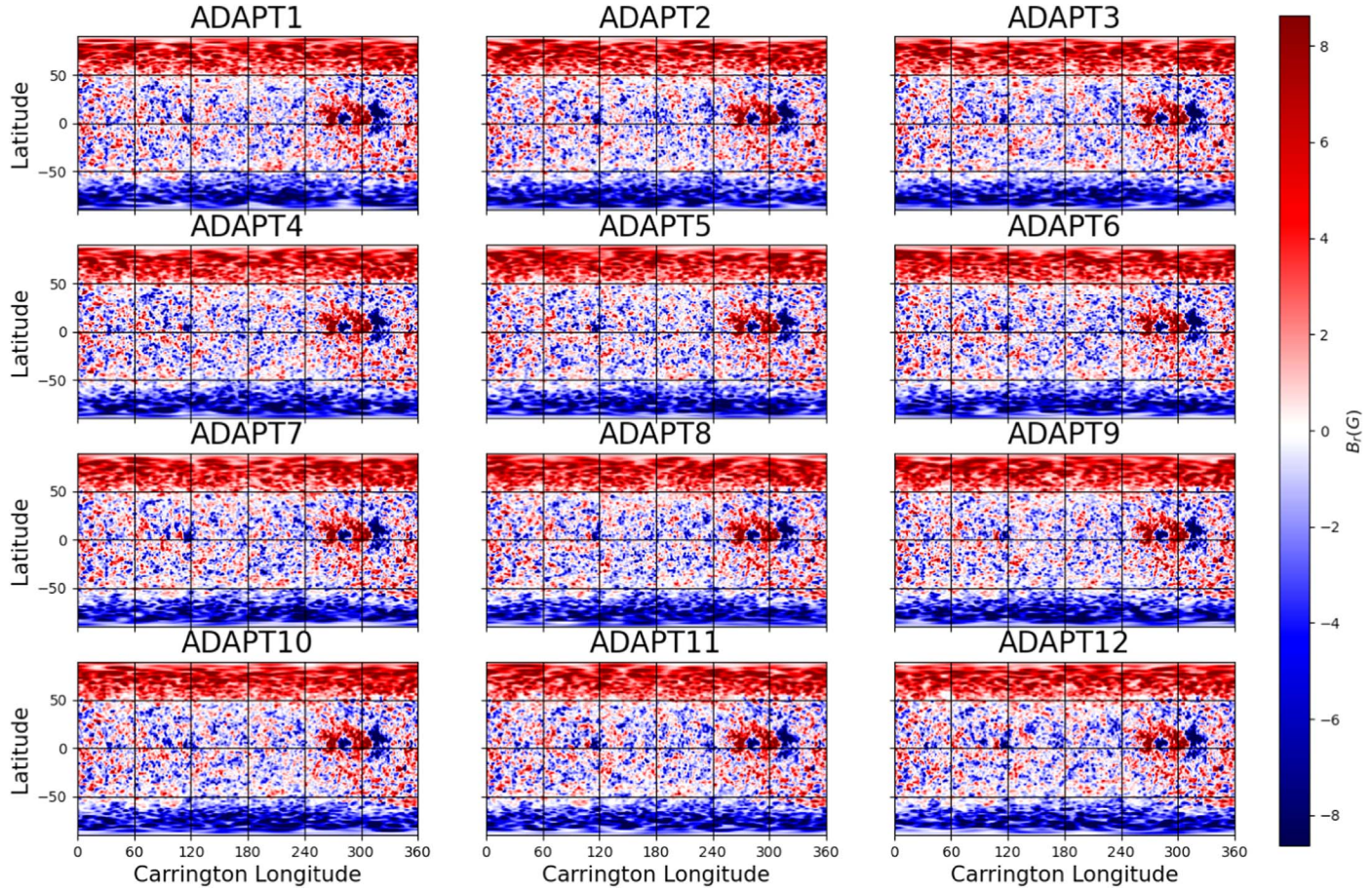

Figure 2. Comparison of the 12 GONG-ADAPT realizations for 2019 July 2 (CR 2219). All data are in their original resolution and axis (longitude–latitude). The ranges of the color bars have been set to plus and minus of the maximum of the field divided by 10, in order to have positive polarities in red and negative polarities in blue, as well as a good balance between small- and large-scale structures.

We use typical solar surface values for the mass density $\rho_\odot = 1.67 \times 10^{-16}$ g cm^{-3} and $T_\odot = 1.9 \times 10^6$ K for fixed-value Dirichlet conditions of density and pressure. The pressure at the inner boundary follows from the solar surface temperature by application of the ideal gas law: $P_\odot = 4.15 \times 10^{-2}$ dyn cm^{-2}.

3.2. Numerical Methods and Boundary Conditions

The state variables are evolved in time using a one-point and three-point implicit backward Euler scheme for steady and unsteady cases (Yalim et al. 2011), respectively, solving the resulting linear system with the generalized minimal residual method (Saad & Schultz 1986), which is implemented within the PETSc library (Balay et al. 1997, 2015a, 2015b).

In order to ensure the divergence constraint $\nabla \cdot \boldsymbol{B} = 0$, we use the artificial compressibility analogy (Chorin 1997), which is very similar to the hyperbolic divergence cleaning method originally developed by Dedner et al. (2002) and has been shown to perform well with our implicit solver (Yalim et al. 2011):

$$\frac{\partial \phi}{\partial t} + V_{\mathrm{ref}}^2 \nabla \cdot \boldsymbol{B} = 0, \tag{2}$$

which couples the zero-divergence constraint to the induction equation, ensuring that the whole system remains purely hyperbolic. c_h denotes the propagation speed of the numerical divergence error, set to 1.0.

The inner velocity is set to 0 at the inner boundary by following the prescription: $V_{x,y,zG} = -V_{x,y,zI}$. This condition allows us to suppress the currents at the solar surface in order to produce a better perfect conductor boundary condition (see Perri et al. 2022 and Brchnelova et al. 2022 for more details).

In order to be able to pass an initial condition for the magnetic field distribution to the MHD solver, we compute a potential field approximation based on a particular magnetic map as an inner (i.e., at the solar surface) boundary condition. From the input synoptic map, we derive a Dirichlet condition based on the radial magnetic field: $B_{r\mathrm{G}} = 2B_{r\mathrm{PF}}|_{\partial\Omega_\mathrm{i}} - B_{r\mathrm{I}}$. Here and in the following, index "G" indicates a value evaluated at a particular ghost cell center, while index "I" refers to the corresponding inner cell, adjacent to the ghost cell. The field value at the ghost cell center is assigned such that the exact boundary value at the cell face bordering ghost- and inner-state symmetrically, e.g., $B_{r\mathrm{PF}}|_{\Omega_\mathrm{i}}$ is the arithmetic mean of the quantity in question as evaluated on the ghost- and inner-state cell centers. $\partial\Omega_\mathrm{i} = \{(r, \vartheta, \varphi) | r = R_\odot\}$ denotes the solar surface boundary and $\partial\Omega_\mathrm{o}$ the outer spherical shell at $r = 21.5\,R_\odot$. Because the other components of the magnetic field are not derived from data, we use simple zero gradient conditions across the inner boundary ($\partial B_\theta/\partial r = \partial B_\varphi/\partial r = 0$).

Due to the solar wind being supersonic at $r = 20.0\,R_\mathrm{S}$, we can extrapolate the spherical field components $r^2 B_r$, B_ϑ, and B_φ, as well as ρ, V_r, V_ϑ, V_φ, and P from the outermost cell centers to the ghost cells with a zero gradient. We extrapolate $r^2 B_r$

Table 2
Summary of the Properties of the GONG Products

Name	Full Name	Frame	Zero-point Correction	Updated Data
mrmqs	Integral Carrington rotation Magnetogram Synoptic Map	Carrington	No	No
mrnqs	Integral synoptic map	Carrington	Yes	No
mrbqs	Standard QuickReduce Magnetogram Synoptic Map	Synchronic	No	No
mrbqj	Janus QuickReduce Magnetogram Synoptic Map	Synchronic	No	Yes
mrzqs	Synoptic map	Synchronic	yes	No

Note. For each product, we explain the full name of the product and the associated frame. We also specify whether the zero-point correction is applied, and whether updated data are included.

instead of B_r to comply with the divergence-free constraint for the magnetic field (see Perri et al. 2018 for more details).

The mesh used for all simulations is a spherical shell domain defined by $\Omega = \{(r, \vartheta, \varphi) | R_\odot < r < 21.5\, R_\odot\}$, where the inner and outer boundary conditions are applied on $r = R_\odot$ and $r = 21.5 R_\odot$, respectively. The surface mesh of a level-six subdivided geodesic polyhedron (consisting of triangular elements) was generated to represent the inner boundary and then extended radially outward in layers until the outer boundary was reached, resulting in a 3D domain consisting of prismatic elements. The default mesh used a sixth-level subdivision of the geodesic polyhedron with 20,480 surface elements, resulting in a grid with 3.9 M elements. One advantage of this mesh is that it does not produce any polar singularity, contrary to most spherical structured meshes. For more details about the mesh design and its impact on the numerical solution, see Brchnelova et al. (2022).

3.3. Input Radial Magnetic Field

Before analyzing the comparison with the observations, we want to first discuss the preprocessing of the synoptic maps, as it will impact the simulation results.

There are two main categories of preprocessing applied to synoptic maps for coronal simulations. PFSS-based models tend to use Gaussian filtering, in combination with a flux-conserved remapping of the map in order to better approximate the poles (Pomoell & Poedts 2018). This preprocessing is important for this kind of method, since the PFSS and the subsequent WSA usually applied afterward are very sensitive to flux distribution and expansion factor. However, for an MHD simulation, we can use another preprocessing: we can do scale filtering by doing a spherical harmonics decomposition and selecting a maximum cutoff frequency, $\ell_{\max}$. This is closer to the techniques used in stellar physics, where the ZDI measurement of the magnetic field usually provides only the first five modes (Vidotto et al. 2018). In this study, we have chosen to apply the same preprocessing to all the maps, with an $\ell_{\max}$ of 15. This is similar to a space-weather operational setup: $\ell_{\max} = 15$ allows us to capture smaller structures like active regions without resolving too refined structures that would slow down the simulation.

In all the following plots, we divide the maps into three categories that we feel are most logical to compare. The first category are the maps in the Carrington frame, which are integral maps. This category concerns WSO, HMI, GONG mrmqs, and GONG mrnqs maps. All of these maps are diachronic, meaning that they are constructed by assembling observations at different times, and thus reflect only approximately the state of the solar surface at a given date. The second category includes the maps with synchronic frames with data that is usually updated daily. This category concerns HMI daily, GONG mrbqs, GONG mrbqj, and GONG mrzqs. These maps have a different reference frame, as the 120° in longitude to the left of the map are replaced with the most recently measured disk data (except for the GONG mrbqs product, which however still uses the same frame). Thus, the central meridian of the chosen date is always placed at 60° from the left side of the map. Finally, we set apart the GONG-ADAPT maps, as they are 12 different variations on the same original GONG data, with just differences in parameters for the applied modeling. The selected GONG-ADAPT maps for this study are also in the Carrington frame, but they are set apart because they are synchronic maps, contrary to the others which are diachronic.

All radial magnetic fields used as boundary conditions can be found in Figure 9 in Appendix A1. The preprocessing smoothens the maps and reduces the differences due to resolution. At the minimum of activity, the maps are dominated by the dipolar configuration with positive polarity at the northern pole going down to 50° in latitude, and a symmetric negative polarity at the southern pole that goes up to −50°. Despite the low activity, an active region is visible, interestingly exactly at the Carrington longitude of the date of interest (around 319°). In order to show a more quantitative comparison between the boundary conditions, we display in Figure 3 the standard deviation as computed for all three of the above-mentioned categories for each pixel, after the input magnetic fields have been interpolated to the medium resolution of 360×180. We have chosen this resolution as it offers a good compromise between the lowest for WSO (73×30) and the highest for HMI data (3600×1440), and also because it is the most common among the chosen maps (GONG and GONG-ADAPT maps already have this resolution). The input field will anyway be interpolated to the unstructured boundary mesh, which is a bit more resolved, at the beginning of the simulation. This shows that at minimum activity, the most significant differences between the input B_r maps are located at the poles and for all three categories: above 60° and below −60° in latitude, Carrington frame diachronic maps have a standard deviation between 1.0 and 1.6, synchronic frame maps between 0.9 and 1.7, and GONG-ADAPT maps between 0.4 and 0.55. We can also note some other sources of differences. For the Carrington frame diachronic maps (panel (a)), there is very good agreement for the edges of the magnetic structures, but a rise in the deviation at the center of the active region. This is probably due to the difference in saturation and resolution of the various maps, which leads to different amplitudes of the magnetic field in the active region. The synchronic frame maps (panel (b)) also show some stronger deviation in the active region, although it is not where the maximum deviation is reached. The GONG-ADAPT maps (panel (c)) have the lowest standard deviation among the three categories, but they exhibit

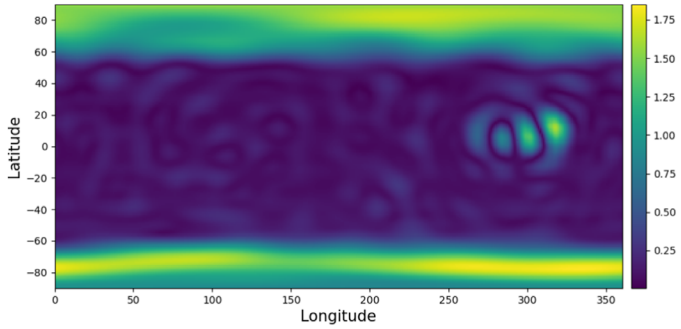

(a) Carrington frame diachronic maps.

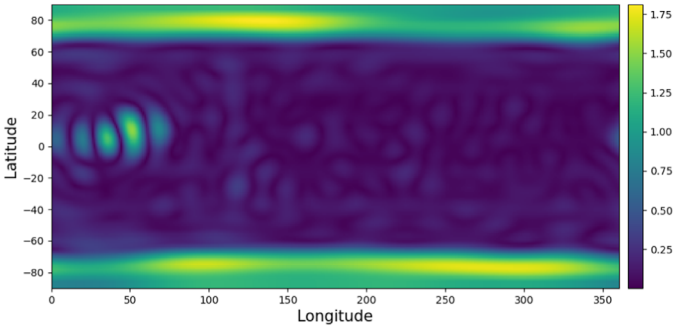

(b) Synchronic frame maps.

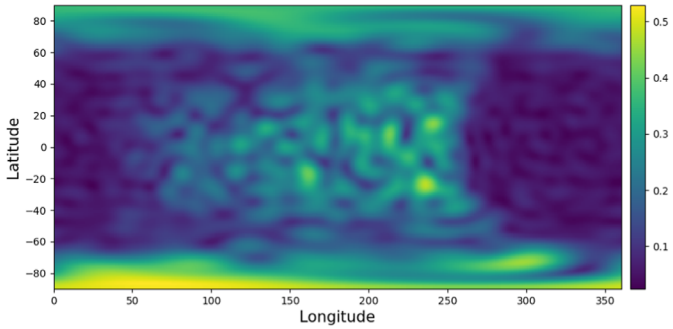

(c) GONG-ADAPT realizations.

Figure 3. Standard deviation for each pixel between input radial magnetic fields derived from magnetic maps. The fields have been interpolated to the medium resolution 360 × 180 for comparison. The first panel shows the standard deviation from the Carrington frame diachronic maps, the second one from synchronic frame maps, and the last one from all 12 GONG-ADAPT realizations for the same map. The corresponding input magnetic fields are shown in Figure 9.

some mild deviation also at the center of the map, which is probably a result of the granulation model that is used and its various parameters that have been tested. The filling of the poles is thus going to be the main factor in explaining the differences that have been observed in the simulations.

4. Comparison of Synoptic Maps for the Minimum of Activity on 2019 July 2

We selected the date of 2019 July 2 because it was the most recent quiet minimum of activity date where we could combine three interesting observations in order to quantify the results of our simulations: a total solar eclipse, visible in South America on this date, provided precise white-light images of the corona, the space observatory SDO took pictures in EUV with its instrument AIA to provide maps of the coronal hole locations, and the space observatory SoHO took a white-light picture with its instrument the Large Angle and Spectrometric Coronagraph Experiment (LASCO) to provide an estimate of the SB location. Although the PSP satellite was launched by this date, it was not close to the Sun at this precise date, making it difficult to provide in situ data in the solar corona (its closest perihelia were on 2019 April 4 and September). In this study, we thus concentrate on remote-sensing comparisons in order to quantify the impact of the choice of the input synoptic map.

4.1. Comparison of the White-light Eclipse Images and the Streamer Edges

The first comparison we show is the comparison between streamer edges and white-light eclipse images. White-light images are usually records of polarization brightness formed by Thomson scattering of photospheric light by coronal free electrons in the K corona (Aschwanden 2004). Outside of solar eclipses, white-light images are generated using a coronograph from a spacecraft (e.g., SOHO/LASCO) or from ground-based observatories (e.g., COSMO/K-COR). The problem with these techniques is that the coronagraph extends above 1 $R_{\odot}$, thus dimming some structures. It is actually during the solar eclipses on Earth that the solar disk is perfectly covered by the Moon, and that we can see the most precisely the shape of the streamers. For this reason, white-light pictures of eclipses have traditionally been used to constrain coronal models (Mikić et al. 1999). They are extremely useful to determine the shape of the streamers in the corona, as they reveal the underlying magnetic field structure. The white-light image we selected for 2019 July 2 is a composite image (128 pictures) from an open database[6] maintained by Miloslav Druckmüller, which has already been used for other studies (Boe et al. 2020).

Some procedures have thus been developed to compare directly the magnetic field lines obtained from simulations with white-light pictures Wagner et al. (2022). This is however limited to the fact that white-light images are 2D projections of the 3D configuration, which makes automatic comparisons challenging. A more quantitative approach relies upon developing a pipeline to produce artificial white-light images from simulations (Mikić et al. 2018). But this approach actually shifts the problem to the modeling of the white-light emission and the filters that are applied post-processing for selecting the right features. In this study, we suggest another approach that

[6] http://www.zam.fme.vutbr.cz/~druck/Eclipse/index.htm

tries to be robust so that it can be automatized, and simple enough to be implemented for all MHD models. What we do is compute the magnetic field lines in our simulations based on 40×40 seeds, which are located on a sphere at $1.01\,R_\odot$. This resolution was chosen as a good compromise between accuracy and speed. Then we select the seeds and corresponding field lines in the plane perpendicular to the observer's LOS on the date of the event. From these, we can extract the largest closed magnetic field line, which then corresponds to the edge of the streamers as seen from Earth. We can finally superpose these edges on the white-light images by projecting the field lines in the 2D plane and adjusting them to the size of the picture (the reference is the radius of the solar disk where we find the conversion between physical and pixel size). The entire procedure is completely automatic and operated by Python scripts.

The results are shown in Figure 4. As stated before, we divide the simulations into three categories based on the frame of the maps (Carrington frame diachronic, synchronic frame, and GONG-ADAPT realizations). For each subgroup, we show the white-light image in grayscale in the background to enhance the features. On top of it, we show the solar disk edge as a red circle. This feature is important because it is actually detected automatically using hysteresis thresholding, and used to adjust the size of the streamers from the simulation to the eclipse picture. Finally, we plot the streamer edges extracted from each simulation in shades of gray. We note that for this date, the streamers are remarkably large, as shown by the white-light image. We can distinguish by eye one streamer on the left, and two streamers on the right that overlap, which probably means that they are not located at the same longitude. At the poles, we can clearly see open magnetic field lines that are almost vertical. This is typical of a minimum of activity configuration. The size of the streamers and the complexity of the structures visible between 1 and 1.5 $R_\odot$ indicate that they may be overarching pseudo-streamers rather than helmet streamers (Wang et al. 2007). These structures are still the most relevant as they indicate the limit between closed and open magnetic field lines. Within each subgroup, we can already see a wide variety of results. For the Carrington frame diachronic maps, the HMI and GONG mrnqs runs yield very good results, but the two other simulations are completely off. The WSO streamers are way too thin, while the GONG mrmqs streamers are shifted upward to a position that no longer matches the white-light image. This is not surprising because GONG mrnqs is supposed to be more accurate than GONG mrmqs thanks to its zero-point correction. For the synchronic frame maps, the best result is given by the HMI run, although the left streamer is too big (5 $R_\odot$ instead of 3.5 $R_\odot$). Between the GONG cases, the best result is given by GONG mrzqs, although the left streamer is too small and shifted too downward. The difference between GONG mrbqs and GONG mrbqj is minimal, with just the right streamers having a better size with GONG mrbqs. This is what we expected, since GONG mrzqs is the most accurate and physical map. It is however surprising that our model performs less efficiently with the synchronic frame maps than with the Carrington frame diachronic maps, which have greater asynchronicity between the data. For the GONG-ADAPT runs, there is greater diversity in the results from that expected based on the standard deviation study, with the left streamer edge ranging from 2.5–3.5 $R_\odot$, and the right streamer from 2–4 $R_\odot$. The overall agreement is still very good, although it is clearly visible that some realizations yield better simulations than others. All results are summed in a more quantitative way in Table 3 (see Section 5.2 for the corresponding discussion).

4.2. Comparison of EUV Images of Coronal Hole Boundaries

The second physical quantity we use for comparison is the EUV emission at 195 Å, which is the wavelength recommended to automatically extract coronal hole boundaries (Badman et al. 2022; Wagner et al. 2022). Coronal holes are dimmings in the EUV emission, which correspond to regions of open magnetic field lines associated with cooler plasma (Cranmer 2009). The synoptic map we use is from the official SDO/AIA website and consists of a reconstruction of the full solar disk based on daily data, following the same principle as the HMI magnetic maps. It has also been remapped to latitude coordinates, which can create some artifacts at the poles due to the LOS constraints. Again, artificial EUV emissions can be generated from simulations to provide an accurate comparison (Lionello et al. 2009; Parenti et al. 2022). The polytropic approximation we use for the coronal heating does not allow us to use such techniques, but we have access to the information about the open magnetic field lines in the simulation. We then proceed to find the boundaries between closed and open field lines at the surface of the star, using a sphere of 400×200 seed points at $1.01\,R_\odot$. We follow the field lines to see if they reach the end of the computational domain at $20\,R_\odot$: if they do, they are open field lines, if not, they are closed field lines. This allows us to retrieve the contours of the open field line regions at the surface of the star, which we can directly compare with the coronal hole synoptic map. This is not completely a direct comparison, as the EUV emission corresponds to the photosphere, while the wind simulations start at the lower corona above the transition region, but we do not have measurements at this height, and assume that the change in structure in the coronal hole is minimal over this interval. Similar comparisons have been performed in previous studies with positive results (Badman et al. 2022).

We plot the results in Figure 5. For each subgroup of the map, we overplot the contours obtained from the various simulations on the synoptic EUV map. At the chosen date, there are mostly polar coronal holes in dark, and also several dimmer equatorial coronal holes at 220°, 270°, and 330° in longitude. The contours from the simulations have to match as closely as possible the contours of these dark regions. For the Carrington frame diachronic maps, we can see that most of the simulations reasonably cover the northern coronal hole, except for the WSO map, which has an incursion toward the equator at 270° in longitude that is not visible in the EUV data. The HMI and GONG mrnqs simulations capture well the southern and equatorial coronal holes, but WSO and GONG mrmqs both overestimate them. Once again, this is not surprising due to the fact that GONG mrnqs is the corrected version of the GONG mrmqs map. For the synchronic frame maps, we observe that the northern and equatorial coronal holes are well captured. The best results for the southern coronal hole are given by the HMI simulation, while all the GONG simulations tend to overestimate it. We can see however the effect of the correction in the GONG mrzqs map, since it is the only GONG map not to exhibit closed field lines at the southern pole. For the GONG-ADAPT simulations, there is little to no disagreement between the different realizations, although the southern coronal hole is

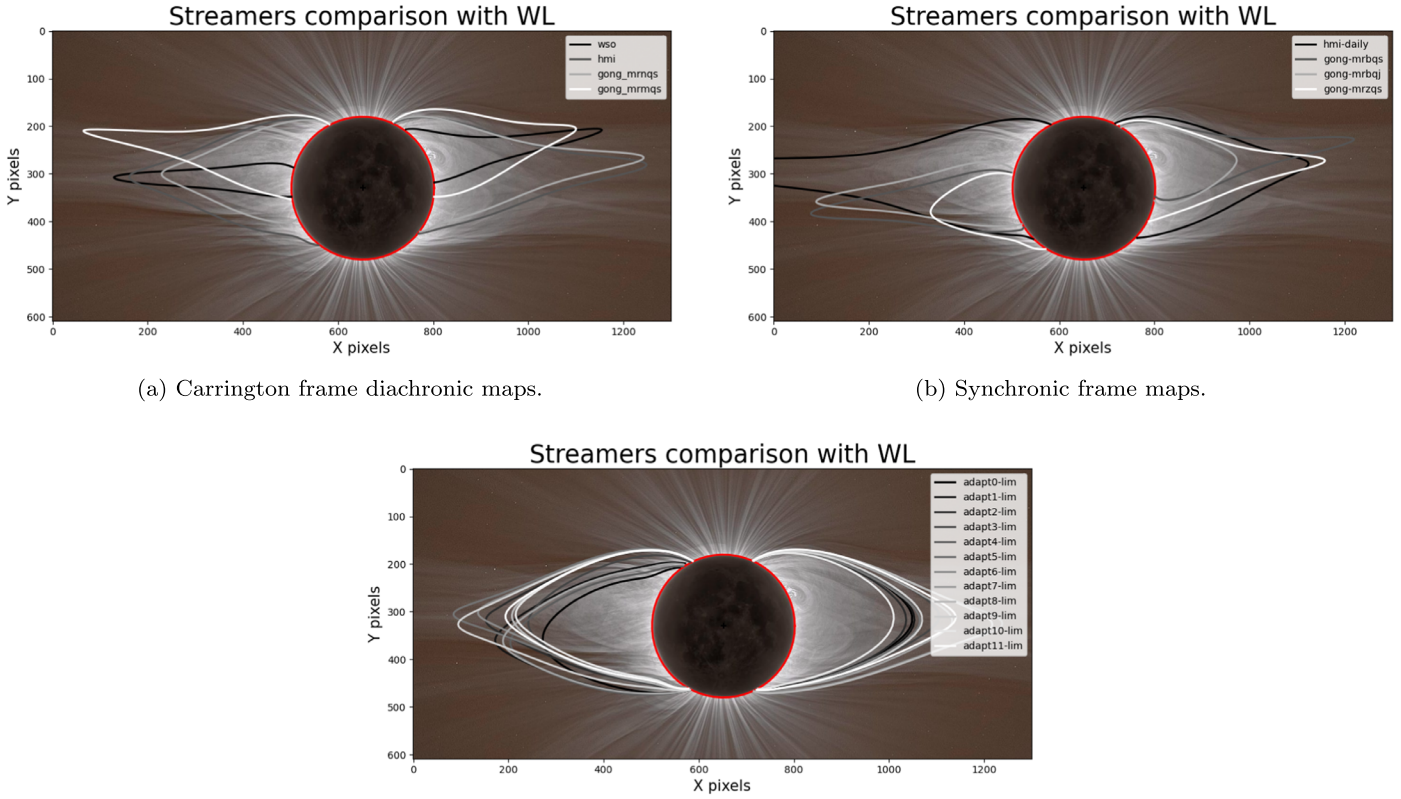

(a) Carrington frame diachronic maps.

(b) Synchronic frame maps.

(c) GONG-ADAPT realisations.

Figure 4. Comparison of the shape of the meridional streamers with the white-light eclipse image from 2019 July 2. The first panel compares the streamers from Carrington frame diachronic maps, the second one from synchronic frame maps, and the last one from all 12 GONG-ADAPT realizations for the same map. The solar disk is highlighted as a red circle as reference. Streamer contours are shown as shades of gray. All streamers have been remapped to the same size ratio using this reference and its conversion to the picture pixels, shown as an axis. Credit for the white-light eclipse images: Peter Aniol and Miloslav Druckmüller.

still the one with the most differences. The agreement is very good for both polar coronal holes, but all realizations completely miss the equatorial coronal holes, which is surprising given the accuracy of the models used and the fact that other maps capture them with the same preprocessing. All results are summed in a more quantitative way in Table 3 (see Section 5.2 for the corresponding discussion).

4.3. Comparison of White-light Coronagraphs of the SB

The last comparison with observational data we want to make is the comparison between the white-light SB and the HCS. The coronagraph LASCO C2 on board SoHO captures white-light images between 1.5 and 6 $R_\odot$. This data can then be assembled as a synoptic map over a Carrington rotation to give an estimate of the SB, which can be assumed to host the HCS and act then as a proxy for it at around 5 $R_\odot$ (Poirier et al. 2021). From the simulations, it is easy to directly extract the HCS, as it is the separation between the positive and negative polarity of the radial magnetic field in the computational domain. Once again, this method has already been used in previous studies with positive results (Badman et al. 2022).

We plot the results in Figure 6. The background shows the white-light synoptic maps in grayscale, with the SB highlighted with a yellow dashed line. Because we are looking at a minimum of activity, the HCS is very flat as the current sheet is almost horizontal, with a slight deviation between 250° and 330° in longitude due to the active region discussed before. The HCS extracted from simulations is plotted as a line in grayscale. For the Carrington frame diachronic runs, we see once again that the HMI and GONG mrnqs simulations yield the best results, although the gap between 250° and 330° in longitude seems more difficult to capture, most probably because of the active region located at this exact spot. The WSO and GONG mrmqs simulations show a shift upward compared to the actual SB, and the WSO simulation shows the largest deviation between 300° and 360° in longitude. For the synchronic frame maps, most of the simulations agree very well, with just a slight overestimation of the SB by the GONG mrbqj simulation. For the GONG-ADAPT realizations, there is also little to no variation between all the various simulations, which capture the SB quite well. The better agreement between simulations can be explained by the fact that this quantity is observed at 5 $R_\odot$, a distance at which the magnetic field is more uniform. All results are summed in a more quantitative way in Table 3 (see Section 5.2 for the corresponding discussion).

5. Space-weather Applications

5.1. Assessing the Impact on Space-weather Forecasting

In an operational setup for space-weather forecasting, the coronal part of the model chain is useful for providing the physical quantities at around 20 $R_\odot$ to heliospheric propagators that can compute them all the way to Earth. Currently, in an operational environment, the coronal part is handled through semiempirical extrapolations, such as the WSA model combined with PFSS and SCS for the magnetic field part (Pomoell & Poedts 2018). This is due to the fact that current

Table 3
Summary of the Comparison between COCONUT MHD Simulations on 2019 July 2 Based on Various Magnetic Maps and the Available Observational Data

Map	Streamers' Ratio	Polar CH Ratio	Equation CH Ratio	SB Deviation
WSO	Left: 28.0% (**−1**), right: 24.0% (**−1**)	North: 72.8% (**−3**), south: 33.7% (**−2**)	10.7% (**−2**)	$\delta_{max} = 30.8°$ (**−1**), $\delta_{mean} = 9.22°$ (**−2**)
HMI	Left: 84.2% (**1**), right: 74.7%	North: 86.1%, south: 40.6%	37.4% (**2**)	$\delta_{max} = 17.5°$, $\delta_{mean} = 4.88°$
GONG (mrmqs)	Left: 54.4%, right: 37.7% (**−3**)	North: 87.1%, south: 23.9% (**−1**)	8.8%	$\delta_{max} = 27.9°$ (**−2**), $\delta_{mean} = 11.9°$ (**−1**)
GONG (mrnqs)	Left: 74.9%, right: 65.6%	North: 86.2%, south: 42.0%	26.2% (**3**)	$\delta_{max} = 19.1°$, $\delta_{mean} = 4.98°$
HMI (sync.)	Left: 66.2%, right: 70.1%	North: 86.3%, south: 40.1%	65.5% (**1**)	$\delta_{max} = 16.1°$, $\delta_{mean} = 4.30°$ (**1**)
GONG (mrbqs)	Left: 39.1% (**−3**), right: 41.6%	North: 80.3% (**−3**), south: 33.9%	11.6%	$\delta_{max} = 23.9°$ (**−3**), $\delta_{mean} = 7.35°$ (**−3**)
GONG (mrbqj)	Left: 47.3%, right: 32.8% (**−2**)	North: 79.2% (**−2**), south: 32.5% (**−2**)	11.4%(**−3**)	$\delta_{max} = 20.5°$, $\delta_{mean} = 6.43°$
GONG (mrzqs)	Left: 29.1% (**−2**), right: 53.6%	North: 85.2%, south: 39.2%	20.4%	$\delta_{max} = 19.7°$, $\delta_{mean} = 4.66°$ (**2**)
ADAPT (1)	Left: 64.3%, right: 77.8%	North: 88.1% (**2**), south: 44.4%	0.0% (**−1**)	$\delta_{max} = 10.5°$, $\delta_{mean} = 5.36°$
ADAPT (2)	Left: 61.7%, right: 77.1%	North: 87.9%, south: 44.1%	0.0% (**−1**)	$\delta_{max} = 9.99°$, $\delta_{mean} = 5.60°$
ADAPT (3)	Left: 69.4%, right: 72.4%	North: 88.3% (**1**), south: 44.0%	0.0% (**−1**)	$\delta_{max} = 10.5°$, $\delta_{mean} = 5.57°$
ADAPT (4)	Left: 77.0% (**3**), right: 85.5% (**3**)	North: 87.9%, south: 43.9%	0.0% (**−1**)	$\delta_{max} = 9.69°$ (**3**), $\delta_{mean} = 4.76°$ (**3**)
ADAPT (5)	Left: 61.4%, right: 79.5%	North: 87.8%, south: 44.5%	0.0% (**−1**)	$\delta_{max} = 9.84°$, $\delta_{mean} = 5.09°$
ADAPT (6)	Left: 66.3%, right: 78.1%	North: 87.5%, south: 44.1%	0.0% (**−1**)	$\delta_{max} = 10.0°$, $\delta_{mean} = 5.84°$
ADAPT (7)	Left: 72.1%, right: 78.5%	North: 87.2%, south: 43.6%	0.0% (**−1**)	$\delta_{max} = 10.4°$, $\delta_{mean} = 6.20°$
ADAPT (8)	Left: 61.9%, right: 87.9% (**1**)	North: 87.4%, south: 45.3% (**1**)	0.0% (**−1**)	$\delta_{max} = 9.63°$ (**2**), $\delta_{mean} = 5.75°$
ADAPT (9)	Left: 75.4%, right: 77.6%	North: 87.7%, south: 43.4%	0.0% (**−1**)	$\delta_{max} = 10.3°$, $\delta_{mean} = 5.91°$
ADAPT (10)	Left: 61.3%, right: 80.5%	North: 88.0% (**3**), south: 44.9% (**2**)	0.0% (**−1**)	$\delta_{max} = 9.39°$ (**1**), $\delta_{mean} = 4.99°$
ADAPT (11)	Left: 80.0% (**2**), right: 64.1%	North: 88.1% (**2**), south: 44.7% (**3**)	0.0% (**−1**)	$\delta_{max} = 10.4°$, $\delta_{mean} = 5.73°$
ADAPT (12)	Left: 76.1%, right: 85.8% (**2**)	North: 87.9%, south: 44.5%	0.0% (**−1**)	$\delta_{max} = 10.0°$, $\delta_{mean} = 5.52°$

Note. We use three quantitative metrics to evaluate the maps: we compute the percentage of overlap between the streamers' edges, the percentage of coverage between the polar and equatorial coronal holes, and the mean and maximum angle of deviation between the SB and the HCS. For more details on the metrics, see Appendix. The best result for each metric is noted (1), the second best is (2), and the third best is (3). The worst result for each metric is symmetrically noted as (−1), the second worse as (−2), and the third worse as (−3). The sync. abbreviation stands for "synchronic frame".

MHD models are too slow to be used in an operational context, although it has been demonstrated on numerous occasions that they are more accurate (Samara et al. 2021). This is a limitation that our code does not have, thanks to its implicit solving method (Perri et al. 2022). It is then interesting to wonder what differences we would observe if we were to couple our MHD model to EUHFORIA, for example, and see the modifications at this interface. As we use a polytropic version of the code for now, it is thus not interesting to do the coupling all the way to Earth because we already know it will not compare well with in situ measurements at L1. However, we can already compare it to typical forecasts. Our velocity, density, and temperature are also going to be limited by the polytropic assumption, so for the moment the best quantity to compare is the radial magnetic field B_r.

We plot the results in Figure 7. The background color shows the radial magnetic field B_r extrapolated at 0.1 au by PFSS +SCS. The positive polarity is shown in red, negative polarity in blue, and the HCS is located at the border between the two. In panels (a) and (c), the PFSS extrapolation is based on the realization 1 from GONG-ADAPT to provide the right frame. At the moment, the prevision models do not offer other maps to work with. In panel (b), it is based on a GONG mrbqs map to have the synchronic frame. We overplot the HCS extracted from our MHD simulations around 0.1 au for comparison. We can see that compared to the HCS at 5 $R_\odot$, the HCS at 0.1 au is not very different, as the global geometry of the magnetic field is already fixed at this distance. We can see however a significant deviation from the HCS from the WSA model. This is surprising for synchronic frame maps, since they are based on exactly the same map for GONG mrbqs, only the model changes. From empirical to MHD, we can see that the gap around the active region is accentuated for the PFSS extrapolation. For the GONG-ADAPT realizations, the MHD model also tends to reduce the north–south variations and flatten the HCS. This is important for space-weather forecasting, as a difference of several tens of degrees at 0.1 au will increase even further and become even more significant at 1 au. It is well known that a southward-inclined IMF B_z for CMEs leads to more geoeffective intense magnetic storms, which means that this difference will have a significant impact on forecasts at Earth (Balan et al. 2014).

5.2. Which Map Should We Choose?

Based on the previous results, we have summarized all our results in Table 3 to create a scoreboard of all the studied maps for this given date with the COCONUT model.

In order to be able to be more quantitative, we have used three metrics based on the comparisons described in the previous section. At first, in order to better compare the streamers' edges, we computed the percentage of overlap between the observations and the simulations. From the white-light eclipse picture, we extracted a visual estimation of the streamers' edges in the plane perpendicular to the observer's LOS. This method is of course limited by the fact that the white-light picture without post-processing offers only a 2D projection of the 3D structure of the streamers. We then identified all the points that are inside the selected contour as belonging to the streamer, and plotted the defined surface along with the streamer from the simulation. We then compute the ratio between the number of pixels that belong to the two streamers (the one from the eclipse picture and the one from the simulation) and the number of pixels within the biggest streamer of the two. This way of computing the ratio allows us to not give a perfect score to simulation streamers that are bigger than the observation streamer

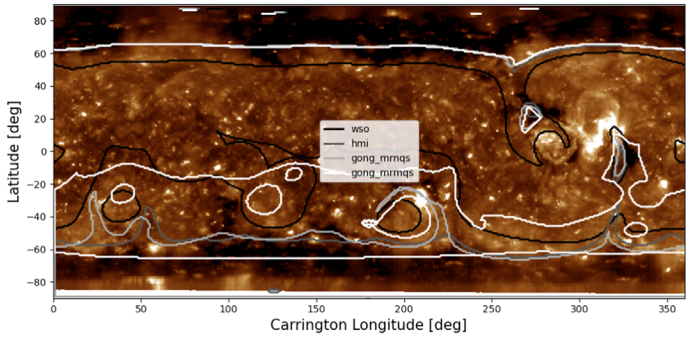

(a) Carrington frame diachronic maps.

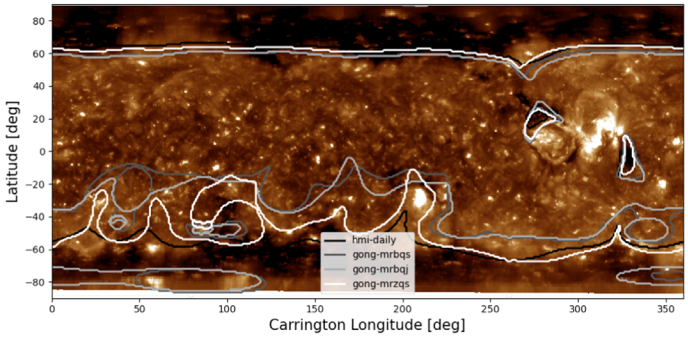

(b) Synchronic frame maps.

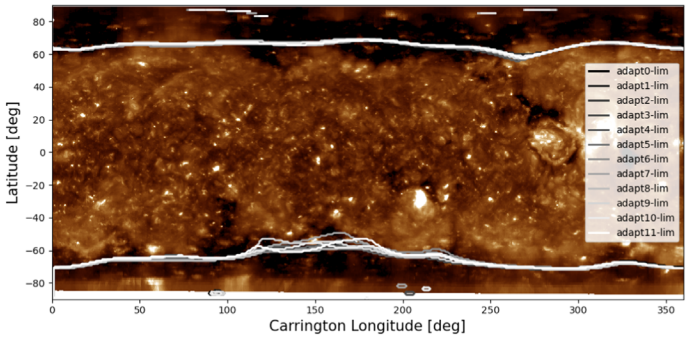

(c) GONG-ADAPT realisations.

Figure 5. Comparison of the contours of the coronal holes with the EUV synoptic map from CR 2219 from SDO/AIA (channel 195). The first panel compares the streamers from Carrington frame diachronic maps, the second one from synchronic frame maps, and the last one from all 12 GONG-ADAPT realizations for the same map. Coronal hole contours from simulations are shown as shades of gray.

and would then include it. The corresponding maps for the computation of this ratio can be found in Figure 10, which provides a visual representation. Then, for the comparison of the coronal holes, we used a similar technique of area ratio. We extracted the pixels that belong to the coronal holes from the EUV synoptic map by applying the EZSEG algorithm developed by Predictive Science Inc. (Caplan et al. 2016). The software is available as part of the EUV2CHM Matlab package from the Predictive Science Inc. website.[7] We converted the algorithm to Python to be able to use it directly on our pipeline for the EUV synoptic map. This algorithm uses an initial intensity threshold to acquire coronal hole locations in a EUV image, and then uses an area-growing technique to define connected regions. This continues until a second intensity threshold is reached, or the condition for connectivity is not met. The dual thresholds and connectivity conditions (essentially the number of consecutive pixels) are defined on input. We experimented with the optimal input parameters, and found that for this map the best result was obtained with a connectivity of 3 neighbors, a first threshold at 20, and a second threshold at 35. The coronal hole for the simulations was determined, as discussed earlier, by using seeds for the field lines and checking whether the field line would reach the outer boundary of the computational domain. We then computed the ratio of the number of pixels in both coronal hole detections to the number of pixels from the coronal holes from the simulation. That way, this percentage represents how accurate the coronal hole from the simulation is. We separated polar and equatorial coronal holes by defining the equatorial region as being between $-40°$ and $40°$ in latitude. The corresponding maps for the computation of this ratio can be found in Figure 11 to have a visual representation. Finally, we compute the deviation of the HCS from the SB. In order to do so, we interpolate the two lines at the same resolution, and compute for each longitude the difference in latitude in degrees. We then process the results to compute the maximum and mean deviation for each map.

Table 3 thus provides an overview of the quality of the maps for this specific date in combination with the current standard setup of the COCONUT model (described in Section 3). What we see is that GONG-ADAPT runs yield very good results for the streamers, the polar coronal holes, and the HCS, but completely fails to capture the equatorial coronal holes. This may be due to the fact that the coronal holes were quite small, but other simulations with different maps managed to capture them with good accuracy with the same preprocessing. This then means that this preprocessing does not work well for our use of the GONG-ADAPT maps with the COCONUT model, and thus should be adapted for these maps. This is important information for forecasts, as equatorial coronal holes are often the sources of high-speed streams that are going to reach Earth and can cause mild space-weather events. The other category of runs that score well are those based on the HMI maps, both the Carrington frame diachronic and synchronic frame. Contrary to the GONG-ADAPT simulations, they have a high score for the equatorial coronal holes, and manage to score high on almost all the metrics. For the GONG runs, the results are overall pretty unsatisfactory, especially for GONG mrbqs and mrbqj, which is surprising because these are the most used maps for

[7] https://www.predsci.com/chd/

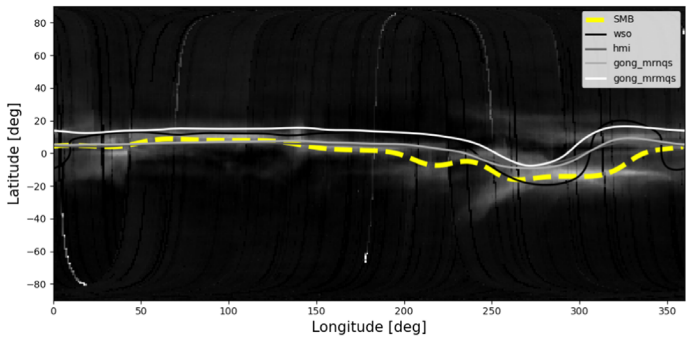

(a) Carrington frame diachronic maps.

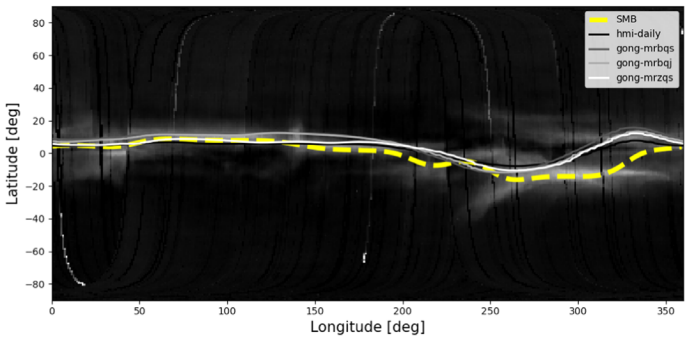

(b) Synchronic frame maps.

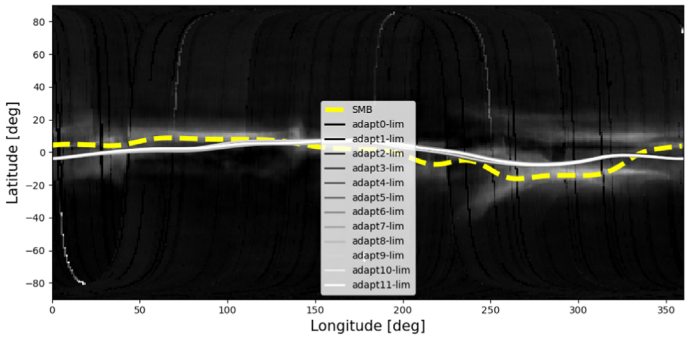

(c) GONG-ADAPT realisations.

Figure 6. Comparison of the shape of the SB with the white-light synoptic maps from 2019 July 2 from SoHO/LASCO/C2. The first panel compares the streamers from Carrington frame diachronic maps, the second one from synchronic frame maps, and the last one from all 12 GONG-ADAPT realizations for the same map. The SMB line inferred from observations is denoted by the yellow dashed line, while the current sheet inferred from simulations is in shades of gray. Credit for the SMB maps: Nicolas Poirier (IRAP).

forecasting. This table gives us some useful guidelines in order to use the COCONUT code for space-weather applications in the most efficient way. From the table, it seems clear that the only acceptable synchronic frame map we could use with COCONUT is GONG mrzqs. Likewise, for the Carrington frame diachronic maps, the correction for the GONG mrnqs map really improves the quality of the simulation. Finally, WSO runs score the worst in almost all the metrics, and are thus not recommended to use as it is with our code. They can however be adjusted with a more elaborate and custom preprocessing, but it is not clear whether this is applicable to space-weather forecasting (Samara et al. 2021).

To conclude, the runs that agree with most of the metrics are the ones based on the GONG-ADAPT maps, although they may require additional preprocessing in order to better treat the equatorial coronal holes. The second-best choice that scores well on average are the HMI simulations, both the Carrington frame diachronic and synchronic frame. This may actually be the best choice for operational previsions with COCONUT, and yet to date few data centers have tested them with other models in operational setups. Instead, the second choice is usually the GONG mrbqs map. For our model, it scores relatively poor (third worse). A better choice for us would be GONG mrzqs for the synchronic frame maps and GONG mrmqs for the Carrington frame diachronic maps. To date, not all prevision centers use the zero-corrected GONG maps, which appear to be better suited since they were designed to provide better results for the solar poles. These conclusions are of course tied to the date and model we used, and would need a more extensive statistical study to be generalized. It is however likely that for the same approximations (ideal MHD and polytropic heating) and similar boundary conditions, other models would find similar results. It would also be interesting to see if the same conclusion holds for a maximum of activity configuration, which would probably show even more disparities between the maps (Yeates et al. 2018). Finally, this is based on remote-sensing coronal validation, and should also be confronted with in situ heliospheric metrics to have a complete view of the impact for space-weather forecasting, but this requires a better description of the coronal heating that we leave for future work.

5.3. Do Solar Poles Matter for Space Weather?

The other point we want to stress is the question of the roles of the solar poles in space-weather forecasts. This is important because most space-weather models actually remove the solar poles, arguing that they are not relevant for forecasts at Earth. However, it has been shown previously that the HCS location for example is very sensitive to the value of the polar field (Svalgaard et al. 1978), and it is an important feature for space-weather forecasting due to its possible interaction with CMEs (Lavraud & Rouillard 2014). It is undeniable that saving precious computational time can help; however, it is essential to quantify the impact of this decision. It may be justified for heliospheric propagators, since the polar boundary condition has little impact on the structures at Earth, but it is way more difficult to be sure for coronal models. That is why we want to focus specifically on this point in our study.

We have shown in Figure 3 that the poles are actually the greatest source of differences between all the various maps at the

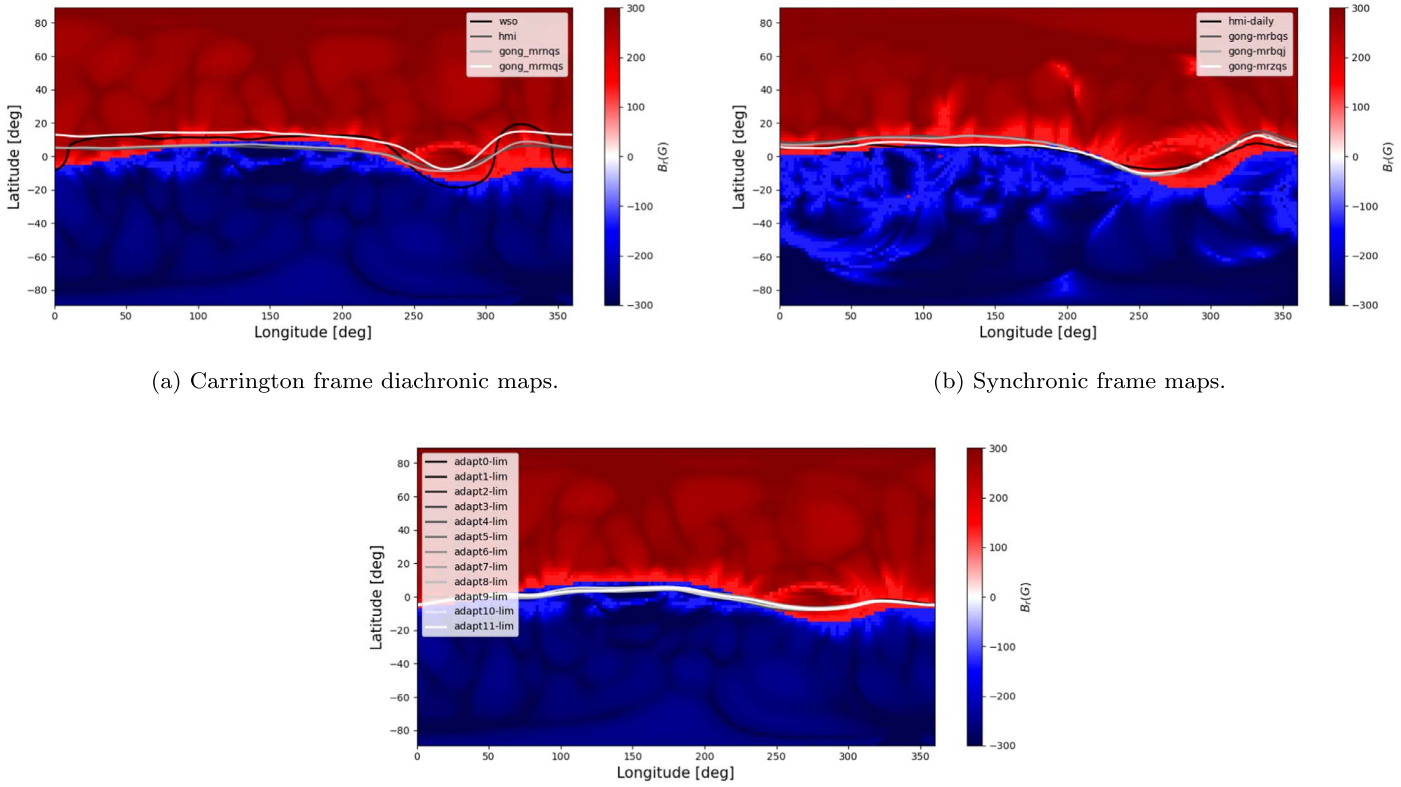

(a) Carrington frame diachronic maps.

(b) Synchronic frame maps.

(c) GONG-ADAPT realisations.

Figure 7. Comparison between the typical HCS extrapolated by a PFSS+SCS method at 0.1 au and the ones extracted from our MHD simulations. The first panel compares the HCS from Carrington frame diachronic maps, the second one from synchronic frame maps, and the last one from all 12 GONG-ADAPT realizations for the same map. The background color shows the radial magnetic field B_r polarity for the extrapolation (red for positive, blue for negative). For panels (a) and (c), the PFSS is based on a GONG-ADAPT map to provide a Carrington rotation frame. For panel (b), it is based on a GONG mrbqs map to provide a synchronic frame.

selected date. To show these differences in a more quantitative way in Figure 8, we perform a 1D cut though all the maps at the Carrington longitude of the date we have chosen, which is around 315° (panels (a), (c), and (e)). We also show the same cut after the preprocessing, to show what is actually used in the simulation (panels (b), (d), and (f)). The main difference is the amplitude of the magnetic field: before the preprocessing, the amplitudes range from −50 to 35 G, while afterward, they range from −9 to 7.5 G. The resolution is also affected as the preprocessing cuts off the smallest spatial structures. The first row (panels (a) and (b)) shows the Carrington frame diachronic maps, the second row (panels (c) and (d)) shows the synchronic frame maps, and the last row (panels (e) and (f)) the GONG-ADAPT realizations. It is already visible from the original maps that the poles exhibit a significant difference, but it is even more dominant after the preprocessing. It is then clear that the maps with which we obtain the best results are the ones that gather more magnetic field at the poles: the GONG-ADAPT maps (panel (f)) because of their flux-transport model, and the HMI maps (orange line in panel (b) and blue line in panel (d)), probably thanks to their high resolution. The GONG zero-corrected products also show some decent magnetic field at the poles (red line in panels (b) and (d)), which probably explains their good scores as well. Bad scores can also be related to bad assessment of polarity at the poles: both WSO and GONG mrmqs (blue and green lines in panel (b)) have extremely inaccurate extrapolations of the poles, with GONG mrmqs even having the wrong polarity at the southern pole, which explains why they get the worse scores. Too much magnetic field at the poles in combination with the numerical diffusion of our model may however lead to underestimating the equatorial regions, as we have seen that GONG-ADAPT runs completely miss the equatorial coronal holes in a typical operational setup (see Figures 5 and 11, and Table 3).

We have shown in Section 4.3 that depending on the input map, our simulations exhibited different shifts of the HCS. Since we have also shown in Section 3.3 that the biggest source of difference between the input maps was the treatment of the solar poles, we can assume that it is an important factor in explaining this shift. It is also expected from Svalgaard et al. (1978) that the magnetic field at the solar poles is going to impact the HCS, causing a shift of several degrees that can completely change its location at 1 au with respect to Earth and hence change the geoeffectiveness and intensity of space-weather events. Most of the differences between the maps we selected at the minimum of activity also came exclusively from the poles, and this had very visible effects on the organization of the corona. In particular, the flux accumulation for the GONG-ADAPT map seems to cause our model in this standard operational setup to miss the equatorial coronal holes contrary to other input maps, which are sources of high-speed streams that hit Earth and trigger space-weather events. This reinforces the importance of the ongoing mission Solar Orbiter, which will be the first imager to capture a global vision of the solar poles, hence helping the filling and calibration of the maps more accurately. With a combination of resolution and accuracy, we can combine the two advantages of HMI and GONG-ADAPT, and thus produce the best map to yield reliable simulations for forecasts.

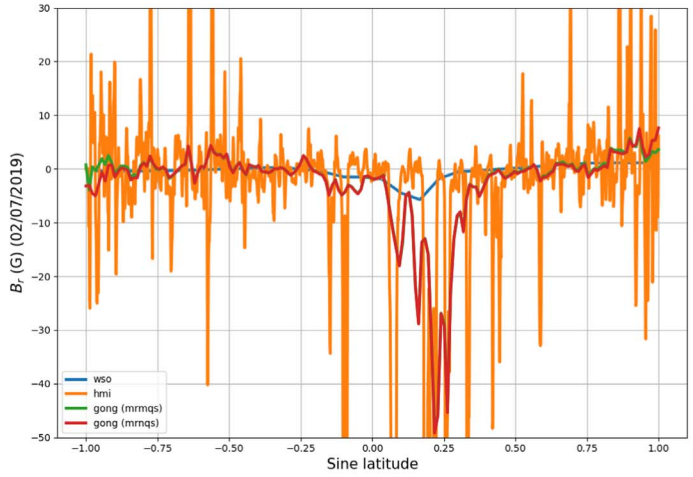

(a) Carrington frame diachronic original maps.

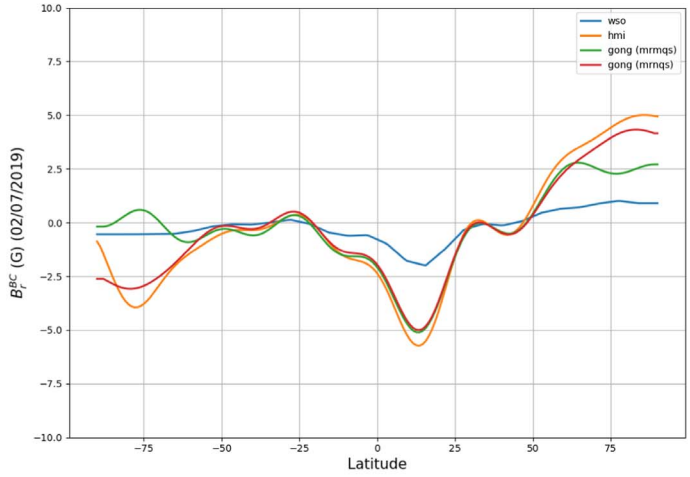

(b) Carrington frame diachronic pre-processed maps.

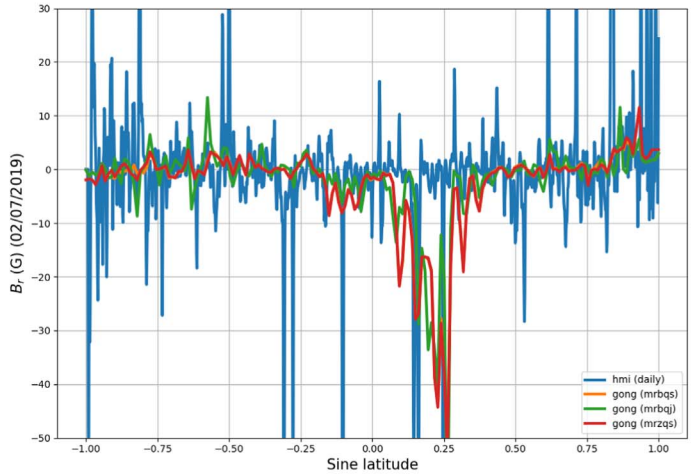

(c) Synchronic frame original maps.

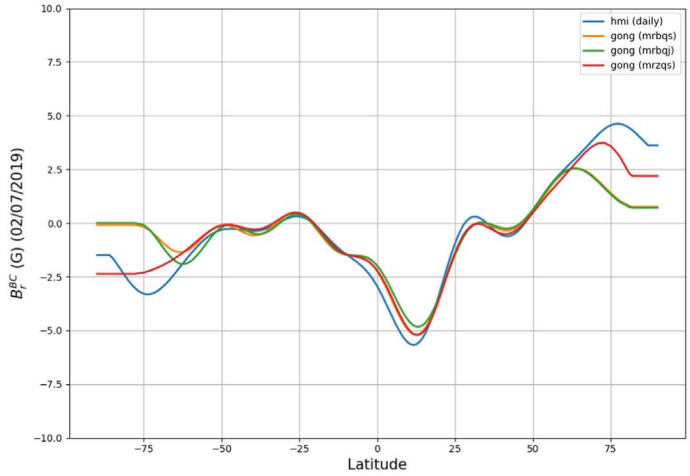

(d) Synchronic frame pre-processed maps.

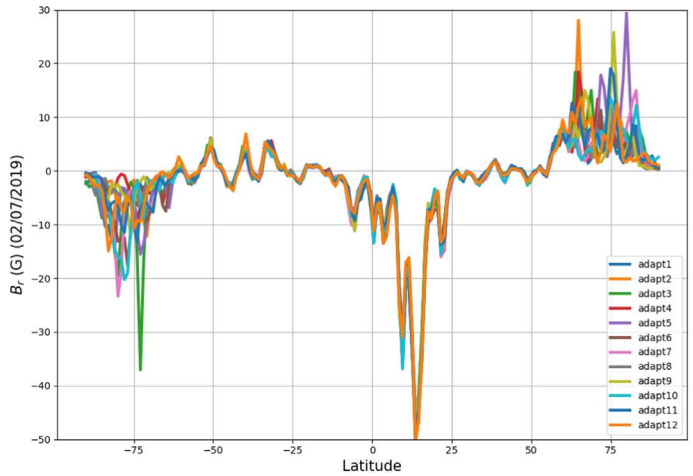

(e) GONG-ADAPT original maps.

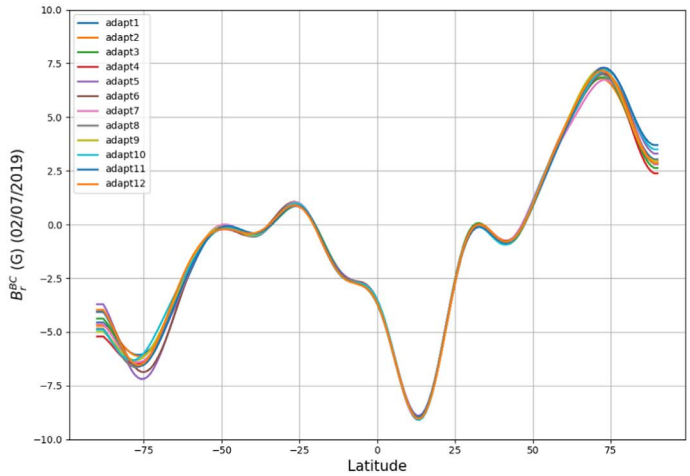

(f) GONG-ADAPT pre-processed maps.

Figure 8. Comparison of 1D cuts of the radial magnetic field B_r at the longitude of the event (2019 July 2). On the left column (panels (a), (c), and (e)), the cuts are made through the original magnetic maps. In the right column (panels (b), (d), and (f)), the cuts are made through the preprocessed maps used as input for the simulations. The first row (panels (a) and (b)) shows the Carrington frame diachronic maps, the second row (panels (c) and (d)) shows the synchronic frame maps, and the last row (panels (e) and (f)) the GONG-ADAPT realizations.

6. Conclusion

We have tested the impact of the choice of the input magnetic map on the results of our coronal solar wind simulations using our new MHD implicit code COCONUT. To this end, we have selected a strategic date (2019 July 2) at the minimum of activity in order to focus on the influence of the solar poles. This choice is recent enough for having a well-documented case and is during a total solar eclipse on Earth, allowing for precise observations of the coronal structures at that time. We gathered all 20 publicly available magnetic maps for this date from four different sources (WSO, HMI, GONG, and GONG-ADAPT), spanning various resolutions and pole-filling techniques. We have preprocessed all maps the same way, with a spherical harmonics cutoff at $\ell_{\max} = 15$, which would be a standard preprocessing in space-weather forecasting operational mode. In order to assess the quality of the resulting simulations, we used three validation techniques with three different remote-sensing observations: we estimated the magnetic field configuration (especially the shape and size of the streamers) from white-light total solar eclipse images, the open magnetic field lines repartition from EUV maps from SDO/AIA, and the position of the HCS using white-light images from SoHO/LASCO/C2. We also computed automatic metrics in order to automatically evaluate the quality of these comparisons.

What we have seen is that our model performs decently when using input from most maps, and allows for a comfortable visual comparison. However, we obtained quite different results depending on the choice of the map, which shows that even at a minimum of activity (i.e., event for quiet configurations) the input data has a strong impact. The quality of estimation for the streamers varies from 24%–85%, with an average quality of about 60%. Coronal holes estimation varies from 24%–88% for the polar coronal holes (with an average of 80% for the northern coronal hole, and 40% for the southern coronal hole), and from 0%–65% for the equatorial ones as some simulations completely fail to reproduce them. The HCS deviation from the SB estimate ranges on average from 4°–12°. We tried to use these results in order to provide guidelines for using our model for space-weather applications, which could probably be extended to other models with similar approximations (ideal MHD and polytropic heating) and boundary conditions. We can already estimate that a similar deviation of the HCS would be observed at 0.1 au, which means that the input boundary condition for heliospheric propagators would definitively be affected. We have also assembled a scoreboard of the performances of our model for each map, which shows that with our model we should not use GONG mrbqs maps as they yield poor results. Instead, a better alternative would be the zero-corrected products such as GONG mrzqs and GONG mrnqs. Runs with GONG-ADAPT products perform very well, except for the equatorial coronal holes, which are not reproduced at all. This could be a major issue for the inclusion of SIRs in the prevision. In the end, the best runs are actually the ones based on the HMI products, which should then become standard inputs for our model when used in space-weather frameworks. We linked these differences to the difference in resolution but also in the treatment of the solar poles, as the flux-transport model from GONG-ADAPT is probably responsible for not reproducing the equatorial coronal holes in this operational setup. This shows that the solar poles are needed to model accurately the first 20 $R_\odot$ and thus cannot be neglected without loss of information. This also highlights the importance of the ongoing Solar Orbiter mission, which will provide more images of the solar poles in order to hopefully unify all these magnetic field measurements.

Of course, this study is just the first step toward better quantifying the requirements for space-weather forecasting. It has proven that our model COCONUT is robust enough to take as input a large variety of maps, and has allowed us to identify the best maps to use to initialize it and provide inputs for space-weather previsions, but there is still the need to see if these results can be generalized. We only studied one minimum of activity, so more cases are needed to reach a conclusion for all minima. Another interesting point is whether these results still hold for the maximum of activity cases: we actually expect the results to potentially vary a lot, since it is not the poles anymore that are driving the simulations, but rather the active regions, so probably that resolution and saturation effects would become more important. It is also not clear if these results hold for other numerical codes, although the previous comparison we did with Wind-Predict would suggest that at least for polytropic models we should find similar results (Perri et al. 2022). We will of course keep improving our model to be able to include more physics: the next key points are the improvement of the modeling for the coronal heating in order to be able to have a bimodal distribution of the solar wind, as well as a multi-fluid treatment to be able to include a realistic transition region up to the chromosphere. Both treatments will help include structures such as SIRs, and thus enable in situ comparisons through coupling with heliospheric propagators such as EUHFORIA. In the end, we hope to be able to prove that our new coronal model not only helps improve space-weather forecasts of wind structures, but also the transients propagating through this description of the interplanetary medium.

The authors would like to thank Nicolas Poirier for providing the white-light SMB maps, and Jasmina Magdalenić for useful discussions. This work has been granted by the AFOSR basic research initiative project FA9550-18-1-0093. This project has also received funding from the European Union's Horizon 2020 research and innovation program under grant agreement No. 870405 (EUHFORIA 2.0) and the ESA project "Heliospheric modeling techniques" (Contract No. 4000133080/20/NL/CRS). F.Z. is supported by a postdoctoral mandate from KU Leuven Internal Funds (PDMT1/21/028). These results were also obtained in the framework of the projects C14/19/089 (C1 project Internal Funds KU Leuven), G.0D07.19N (FWO-Vlaanderen), SIDC Data Exploitation (ESA Prodex-12), and Belspo projects BR/165/A2/CCSOM and B2/191/P1/SWiM. The resources and services used in this work were provided by the VSC (Flemish Supercomputer Centre), funded by the Research Foundation—Flanders (FWO) and the Flemish Government. Wilcox Solar Observatory data used in this study was obtained via the website http://wso.stanford.edu courtesy of J.T. Hoeksema. The Wilcox Solar Observatory is currently supported by NASA. Data were acquired by GONG instruments operated by NISP/NSO/AURA/NSF with contribution from NOAA. HMI data are courtesy of the Joint Science Operations Center (JSOC) Science Data Processing team at Stanford University. This work utilizes data produced collaboratively between AFRL/ADAPT and NSO/NISP. Data used in this study was obtained from the following websites: WSO: http://wso.stanford.edu/synopticl.html GONG: https://gong2.nso.edu/archive/patch.

pl?menutype=z HMI: http://jsoc.stanford.edu/HMI/LOS_Synoptic_charts.html GONG-ADAPT: https://gong.nso.edu/adapt/maps/

Appendix
Complementary Metric Plots

In this appendix, we present some complementary plots that are briefly mentioned throughout the paper. The reason they were not included in the main paper is because they were too voluminous, with each time 20 subplots for the 20 cases considered.

A1. Input Radial Magnetic Field Maps

In Section 2, we presented the various magnetic maps used for our simulations. However, as explained in Section 3.3, we do not directly use the maps as they are; instead, we apply a preprocessing step to them in order to use them as input in our code. We use standard automatic preprocessing to simulate an operational framework without any optimization. To this end, we apply spherical harmonics filtering with a cutoff at $\ell_{\max} = 15$. This results in the modified synoptic maps visible in Figure 9. For each case, we show the resulting radial magnetic field B_r map used directly as input to our simulations. We can see that the preprocessing smoothens the differences in resolution, with now only the WSO map showing a significant difference. This also reduces the difference in amplitude of the magnetic field: before, the maximum amplitude went up to 50 G with the HMI map, while now it reaches only 3 G for the GONG-ADAPT maps. This is because the preprocessing we chose cuts off the contribution of the small-scale structures that correspond to the active region. This allows us to focus more on the effects of the poles, as we wanted.

A2. Overlapping Streamer Maps

In Section 4.1, we qualitatively compared the shape of the streamers we obtained from our MHD simulations to total solar eclipse white-light images that allow estimating such structures. In Section 5.2, we compiled a more quantitative score to be able to evaluate each map's performance. We have explained the principle behind this metric, which is shown in Figure 10. From the white-light image, we can extract a visual estimation of the shapes of the two streamers that are perpendicular to the LOS. Then, we can compare it to the shape of the streamers extracted automatically from our numerical simulations by selecting the biggest closed magnetic field lines. We can then detect which pixel belongs within each streamer and obtain the maps shown in Figure 10: if a pixel does not belong to any streamer, it is in purple; if it belongs to one streamer only, it is in green; if it belongs to both streamers (from the observations and from the simulations), it is in yellow. We then compare the percentage of yellow pixels with the number of pixels within the biggest streamer between observation and simulation. This allows us to avoid the case where the simulation streamers include the observation streamer, which would yield 100% coverage while some of the detection is false. If the observation streamer is bigger, then we compute the percentage of pixels detected. If the simulation streamer is bigger, then we compute the percentage of right detection over false detection. Of course, we would get a better estimate if there was a way to detect automatically the streamer's edge in the white-light picture, but the 3D projection to a 2D picture makes it still very challenging (Boe et al. 2020). The next step would be to directly generate white-light emissions from the simulations, although this raises new problems linked to the emission functions selected and the filters applied afterward to see the structures (Mikić et al. 2018). Our procedure has the advantage of being semiautomatic and very universal since it relies directly on the magnetic field provided by the simulations.

A3. Overlapping Coronal Hole Maps

In Section 4.2, we visually compared the repartition of open magnetic field lines at the surface of the star with coronal hole maps derived from EUV emission from SDO/AIA (195 Åchannel). In Section 5.2, we once again needed a more quantitative metric to be able to evaluate the performance of each map. To do so, we first have to be able to extract automatically the pixels that belong to the coronal holes. We have done so by applying the EZSEG algorithm developed by Predictive Science Inc. (Caplan et al. 2016). The software is available as part of the EUV2CHM Matlab package from the Predictive Science Inc. website.[8] We converted the algorithm to Python to be able to use it directly on our pipeline for the EUV synoptic map. This algorithm uses an initial intensity threshold to acquire coronal hole locations in a EUV image, and then uses an area-growing technique to define connected regions. This continues until a second intensity threshold is reached, or the condition for connectivity is not met. The dual thresholds and connectivity conditions (essentially the number of consecutive pixels) are defined on input. We experimented with the optimal input parameters, and found that for this map the best result was obtained with a connectivity of 3 neighbors, a first threshold at 20, and a second threshold at 35. The resulting coronal hole detection can be seen in gray in all the panels in Figure 11. As discussed previously, the coronal hole for the simulations was determined before by using seeds for the field lines and checking whether the field line would reach the outer boundary of the computational domain. With the simulation we can even link our coronal holes back to the polarity of the magnetic field. In Figure 11, we can then show the contours of our artificial coronal holes in red for associated positive polarity and in blue for negatively associated polarity. We then computed the ratio of the number of pixels in both coronal hole detections to the number of pixels from the coronal holes from the simulation. That way, this percentage represents how accurate the coronal hole from the simulation is. We separated polar and equatorial coronal holes by defining the equatorial region as being between $-40°$ and $40°$ in latitude. The quality of our comparison is limited by two factors. First, the EUV synoptic map has been reprojected from sinus latitudes to equally spaced latitudes, which can generate some uncertainties at the poles. It seems that the southern pole in particular is badly affected, as can be seen in Figure 5, which would explain why the southern coronal hole seems more disrupted and generates poor scores. We are also limited by the preprocessing of the input map, which removes some small-scale structures, but that way we are closer to operational results.

[8] https://www.predsci.com/chd/

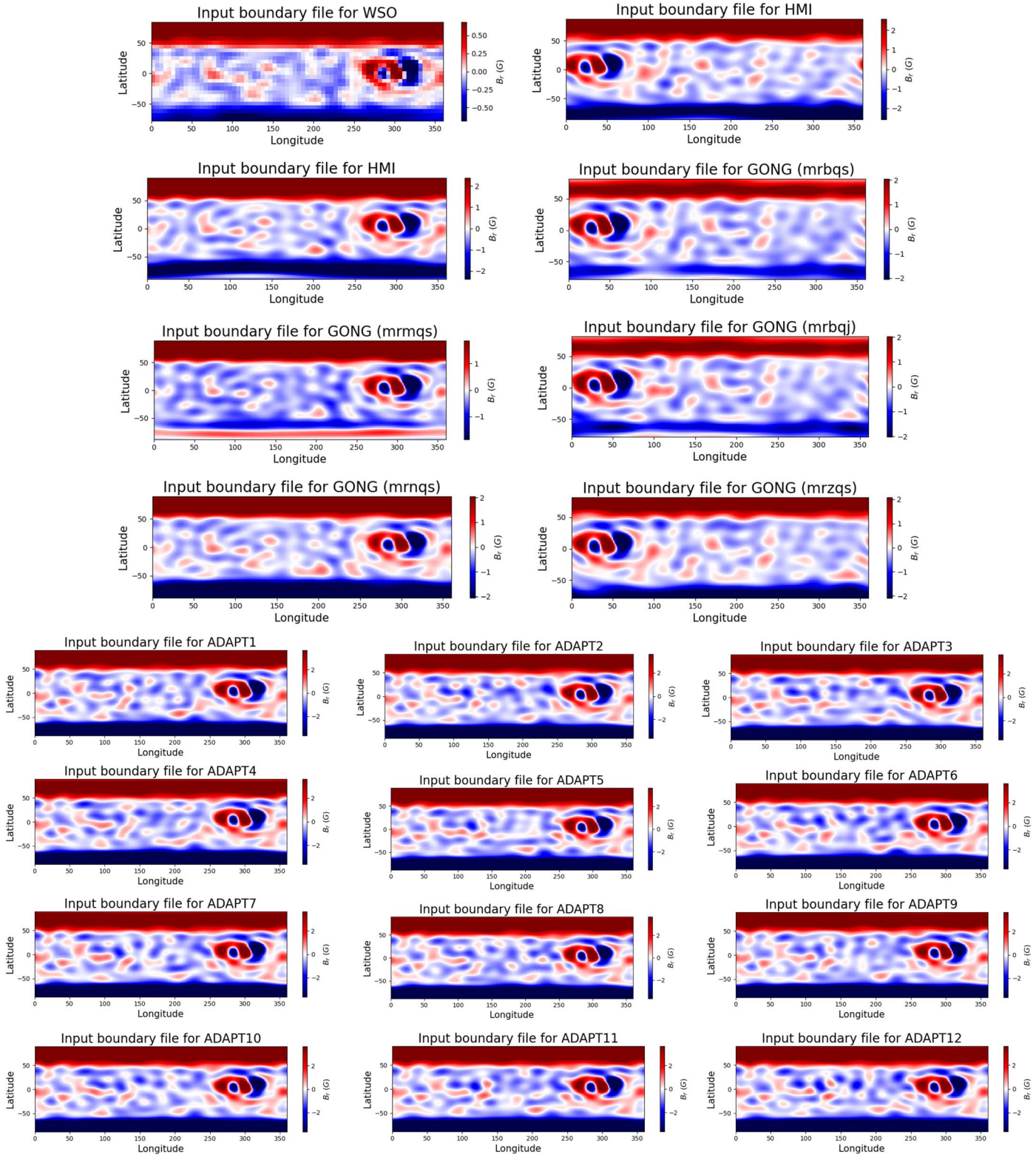

Figure 9. Radial magnetic field B_r, which is used as an input boundary condition for the simulations after applying the map preprocessing. All maps shown here have been smoothened using a spherical harmonics decomposition with $\ell_{\max} = 15$. The column at the top left shows maps in Carrington diachronic frame, the column at the top right maps in the synchronic frame, and the final block at the bottom shows all 12 realizations from the same GONG-ADAPT map. The color bar has been adjusted to show positive magnetic polarity in red, and negative polarity in blue. Each subplot has its own color bar to better show the differences in amplitude between the input fields.

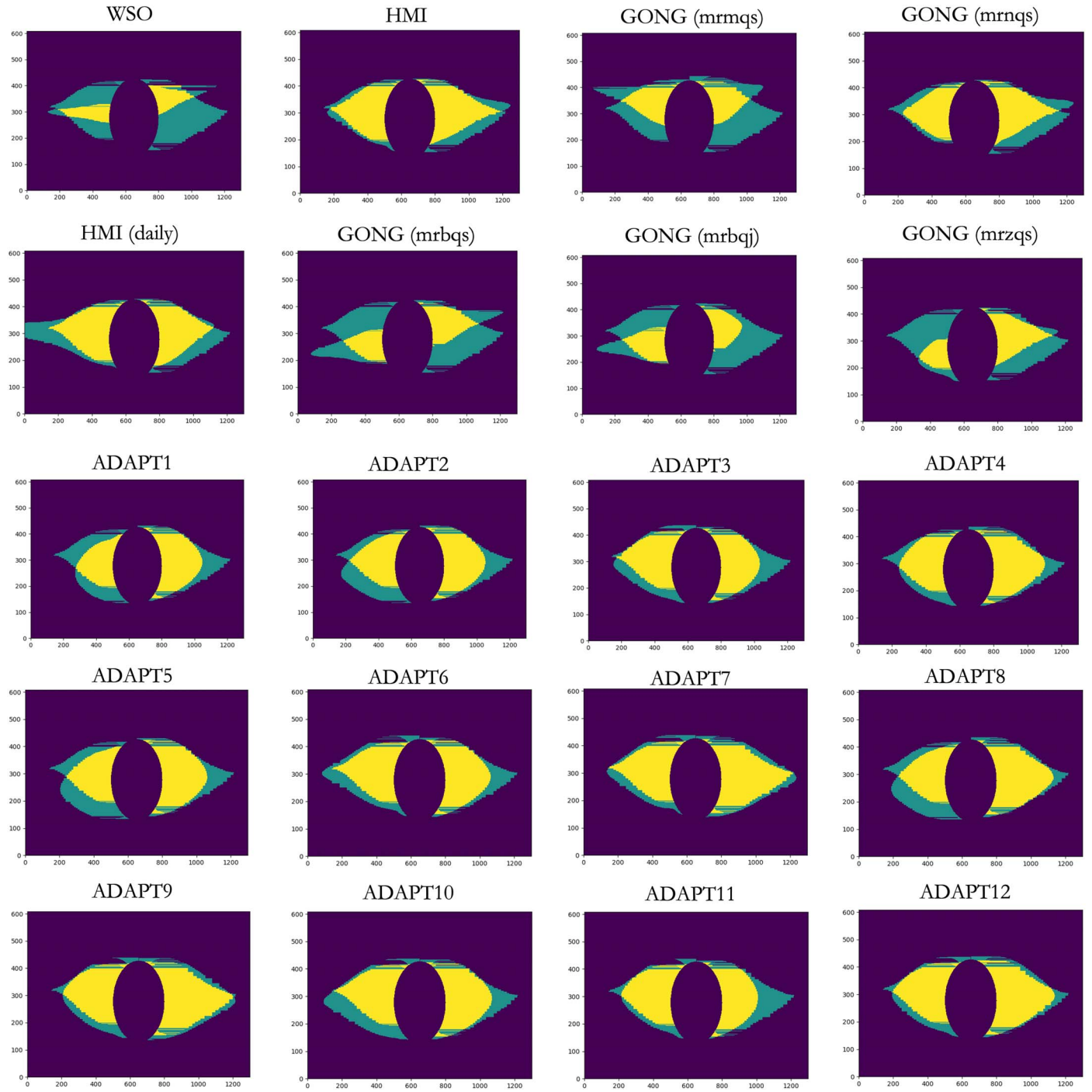

Figure 10. Maps of the streamers' coverage computation for each map simulation. An estimation of the streamer edges in the plane perpendicular to the observer's LOS is extracted manually from the white-light image of the eclipse and plotted with the streamer extracted from the simulation. Each pixel that does not belong within any of the streamers is in purple. Each pixel that belongs to one streamer is in green. Each pixel that belongs to the two streamers is in yellow.

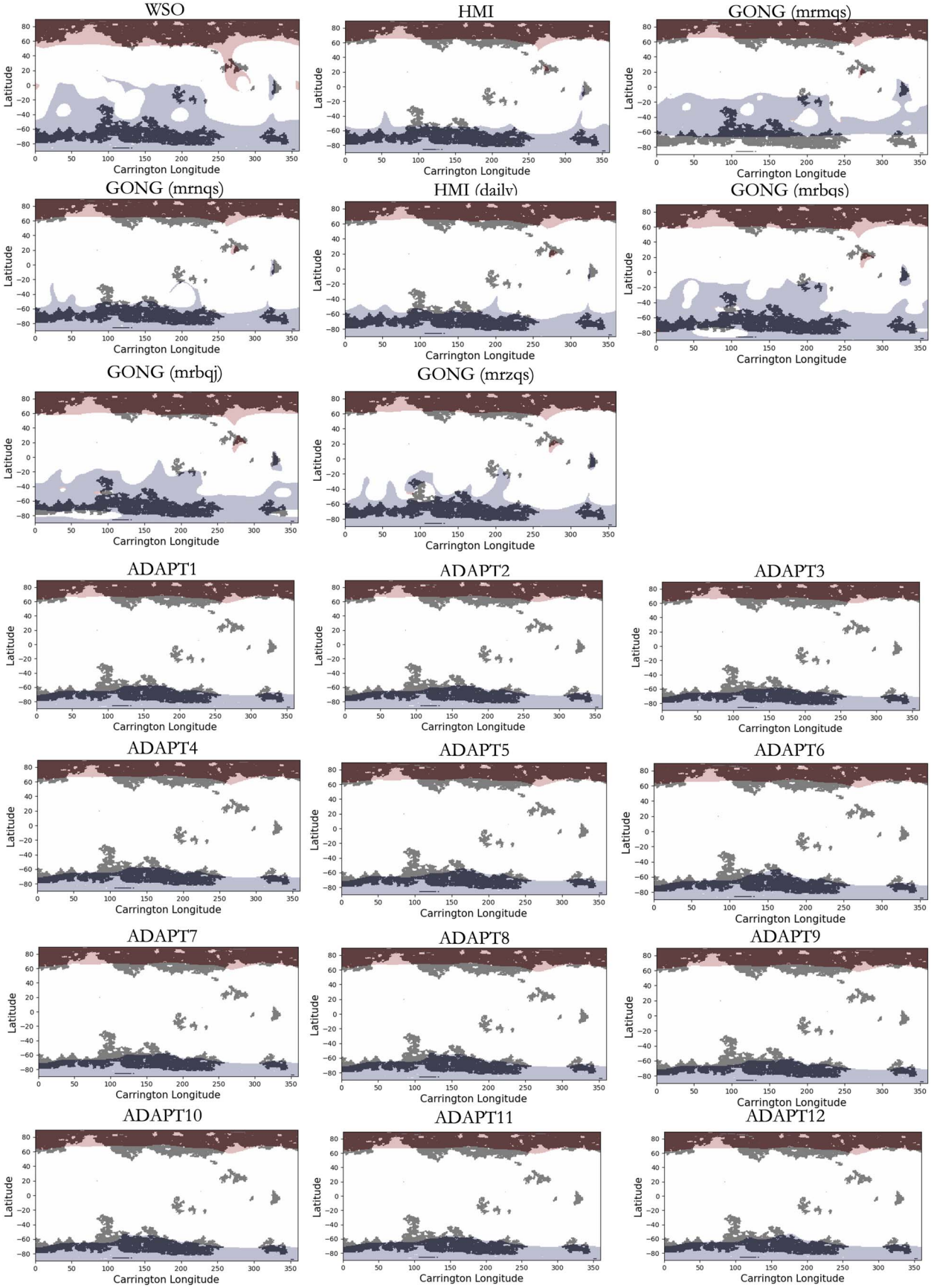

Figure 11. Comparison between the coronal holes extracted from the EUV synoptic map and the MHD simulations for each map. The coronal hole contours are extracted using the EZSEG algorithm and plotted in gray. The coronal holes from the simulations are plotted in red (for positive polarity) and blue (for negative polarity).

ORCID iDs

Barbara Perri https://orcid.org/0000-0002-2137-2896
Błażej Kuźma https://orcid.org/0000-0001-9438-9333
Michaela Brchnelova https://orcid.org/0000-0003-0874-2669
Tinatin Baratashvili https://orcid.org/0000-0002-1986-4496
Fan Zhang https://orcid.org/0000-0002-9425-994X
Peter Leitner https://orcid.org/0000-0003-3792-0452
Andrea Lani https://orcid.org/0000-0003-4017-215X
Stefaan Poedts https://orcid.org/0000-0002-1743-0651

References

Alonso Asensio, I., Alvarez Laguna, A., Aissa, M. H., et al. 2019, CoPhC, 239, 16
Alvarez Laguna, A., Lani, A., Deconinck, H., Mansour, N., & Poedts, S. 2016, JCoPh, 318, 252
Alvarez Laguna, A., Ozak, N., Lani, A., et al. 2019, JPhCS, 1031, 011001
Aschwanden, M. J. 2004, Physics of the Solar Corona. An Introduction (Chichester: Praxis Publishing)
Badman, S. T., Brooks, D. H., Poirier, N., et al. 2022, ApJ, 932, 135
Balan, N., Skoug, R., Tulasi Ram, S., et al. 2014, JGRE, 119, 10041
Balay, S., Abhyankar, S., Adams, M. F., et al. 2015a, PETSc Web page, http://www.mcs.anl.gov/petsc
Balay, S., Abhyankar, S., Adams, M. F., et al. 2015b, PETSc Users Manual Tech. Rep. ANL-95/11—Rev. 3.6, Argonne National Laboratory, http://www.mcs.anl.gov/petsc
Balay, S., Gropp, W. D., McInnes, L. C., & Smith, B. F. 1997, in Modern Software Tools in Scientific Computing, ed. E. Arge, A. M. Bruaset, & H. P. Langtangen (Berlin: Springer), 163
Boe, B., Habbal, S., & Druckmüller, M. 2020, ApJ, 895, 123
Bothmer, V., & Daglis, I. A. 2007, Space Weather: Physics and Effects (Chichester: Praxis Publishing)
Brchnelova, M., Perri, B., Brchnelova, M., et al. 2022, JPlPh, 88, 905880205
Brun, A. S., & Browning, M. K. 2017, LRSP, 14, 4
Caplan, R. M., Downs, C., & Linker, J. A. 2016, ApJ, 823, 53
Caplan, R. M., Downs, C., Linker, J. A., & Mikic, Z. 2021, ApJ, 915, 44
Chhiber, R., Usmanov, A. V., Matthaeus, W. H., & Goldstein, M. L. 2021, ApJ, 923, 89
Chorin, A. J. 1997, JCoPh, 135, 118
Cranmer, S. R. 2009, LRSP, 6, 3
Cranmer, S. R., & Winebarger, A. R. 2019, ARA&A, 57, 157
Dedner, A., Kemm, F., Kröner, D., et al. 2002, JCoPh, 175, 645
Fargette, N., Lavraud, B., Rouillard, A. P., et al. 2021, ApJ, 919, 96
Gopalswamy, N., Yashiro, S., Mäkelä, P., et al. 2012, ApJL, 750, L42
Hickmann, K. S., Godinez, H. C., Henney, C. J., & Arge, C. N. 2015, SoPh, 290, 1105
Ito, H., Tsuneta, S., Shiota, D., Tokumaru, M., & Fujiki, K. 2010, ApJ, 719, 131
Jian, L. K., MacNeice, P. J., Taktakishvili, A., et al. 2015, SpWea, 13, 316
Jin, M., Nitta, N. V., & Cohen, C. M. S. 2022, SpWea, 20, e2021SW002894
Kimpe, D., Lani, A., Quintino, T., Poedts, S., & Vandewalle, S. 2005, in Recent Advances in Parallel Virtual Machine and Message Passing Interface, ed. B. Di Martino, D. Kranzlmüller, & J. Dongarra (Berlin: Springer), 520
Lani, A., Quintino, T., Kimpe, D., et al. 2005, in Computational Science—ICCS 2005, ed. G. D. van Albada, P. M. A. Sloot, & J. J. Dongarra (Berlin Heidelberg: Springer), 279
Lani, A., Quintino, T., Kimpe, D., et al. 2006, Sci. Program., 14, 393058
Lani, A., Villedieu, N., Bensassi, K., et al. 2013, in 21st AIAA CFD Conf., AIAA 2013–2589 (Reston, VA: AIAA)
Lani, A., Yalim, M. S., & Poedts, S. 2014, CoPhC, 185, 2538
Lavraud, B., & Rouillard, A. 2014, in IAU Symp. 300, Nature of Prominences and Their Role in Space Weather (Cambridge: Cambridge Univ. Press), 273
Li, H., Feng, X., & Wei, F. 2021, JGRA, 126, e28870
Linker, J. A., Caplan, R. M., Downs, C., et al. 2017, ApJ, 848, 70
Lionello, R., Linker, J. A., & Mikić, Z. 2009, ApJ, 690, 902
Maneva, Y. G., Laguna, A. A., Lani, A., & Poedts, S. 2017, ApJ, 836, 197
McComas, D. J., Ebert, R. W., Elliott, H. A., et al. 2008, GeoRL, 35, L18103
McComas, D. J., Elliott, H. A., Schwadron, N. A., et al. 2003, GeoRL, 30, 1517
Mikić, Z., Downs, C., Linker, J. A., et al. 2018, NatAs, 2, 913
Mikić, Z., Linker, J. A., Schnack, D. D., Lionello, R., & Tarditi, A. 1999, PhPl, 6, 2217
Odstrcil, D. 2003, AdSpR, 32, 497
Owens, M. J., & Forsyth, R. J. 2013, LRSP, 10, 5
Owens, M. J., Spence, H. E., McGregor, S., et al. 2008, SpWea, 6, S08001
Parenti, S., Réville, V., Brun, A. S., et al. 2022, ApJ, 929, 75
Perri, B., Brun, A. S., Réville, V., & Strugarek, A. 2018, JPlPh, 84, 765840501
Perri, B., Leitner, P., Brchnelova, M., et al. 2022, ApJ, 263, 18
Petrie, G. J. D. 2013, ApJ, 768, 162
Petrie, G. J. D. 2015, LRSP, 12, 5
Pinto, R. F., & Rouillard, A. P. 2017, ApJ, 838, 89
Pirjola, R. 2005, AdSpR, 36, 2231
Poedts, S., Kochanov, A., Lani, A., et al. 2020a, JSWSC, 10, 14
Poedts, S., Lani, A., Scolini, C., et al. 2020b, JSWSC, 10, 57
Poirier, N., Rouillard, A. P., Kouloumvakos, A., et al. 2021, FrASS, 8, 84
Pomoell, J., & Poedts, S. 2018, JSWSC, 8, A35
Pulkkinen, T. 2007, LRSP, 4, 1
Reames, D. V. 2013, SSRv, 175, 53
Reames, D. V. 2021, Solar Energetic Particles: A Modern Primer on Understanding Sources, Acceleration and Propagation, 978 (Berlin: Springer)
Réville, V., Brun, A. S., Strugarek, A., et al. 2015, ApJ, 814, 99
Réville, V., Velli, M., Panasenco, O., et al. 2020, ApJS, 246, 24
Riley, P., & Ben-Nun, M. 2021, SpWea, 19, e02775
Riley, P., Ben-Nun, M., Linker, J. A., et al. 2014, SoPh, 289, 769
Riley, P., Linker, J. A., Mikic, Z., et al. 2019, ApJ, 884, 18
Saad, Y., & Schultz, M. H. 1986, SJSC, 7, 856
Samara, E., Laperre, B., Kieokaew, R., et al. 2022, ApJ, 927, 187
Samara, E., Pinto, R. F., Magdalenić, J., et al. 2021, A&A, 648, A35
Schrijver, C. J., Kauristie, K., Aylward, A. D., et al. 2015, AdSpR, 55, 2745
Shen, F., Shen, C., Xu, M., et al. 2022, RvMPP, 6, 8
Shiota, D., Kataoka, R., Miyoshi, Y., et al. 2014, SpWea, 12, 187
Singh, T., Yalim, M. S., & Pogorelov, N. V. 2018, ApJ, 864, 18
Svalgaard, L. 2006, in 2006 SHINE Workshop (Washington, DC: NASA)
Svalgaard, L., Duvall, T. L. J., & Scherrer, P. H. 1978, SoPh, 58, 225
Temmer, M. 2021, LRSP, 18, 4
Tóth, G., van der Holst, B., Sokolov, I. V., et al. 2012, JCoPh, 231, 870
Tsuneta, S., Ichimoto, K., Katsukawa, Y., et al. 2008, ApJ, 688, 1374
Ulrich, R. K. 1992, in ASP Conf. Ser., 26, Cool Stars, Stellar Systems, and the Sun, ed. M. S. Giampapa & J. A. Bookbinder (San Francisco, CA: ASP), 265
van der Holst, B., Sokolov, I. V., Meng, X., et al. 2014, ApJ, 782, 81
Vidotto, A. A., Lehmann, L. T., Jardine, M., & Pevtsov, A. A. 2018, MNRAS, 480, 477
Virtanen, I., & Mursula, K. 2017, A&A, 604, A7
Wagner, A., Asvestari, E., Temmer, M., Heinemann, S. G., & Pomoell, J. 2022, A&A, 657, A117
Wallace, S., Arge, C. N., Pattichis, M., Hock-Mysliwiec, R. A., & Henney, C. J. 2019, SoPh, 294, 19
Wang, Y. M., Sheeley, N. R. J., & Rich, N. B. 2007, ApJ, 658, 1340
Wu, S. T., Wang, A. H., Liu, Y., & Hoeksema, J. T. 2006, ApJ, 652, 800
Yalim, M. S., Pogorelov, N., Singh, T., & Liu, Y. 2017, AGU Fall Meeting Abstracts, 2017, SH23D–2698
Yalim, M. S., Vanden Abeele, D., Lani, A., Quintino, T., & Deconinck, H. 2011, JCoPh, 230, 6136
Yeates, A. R., Amari, T., Contopoulos, I., et al. 2018, SSRv, 214, 99